AGU ADVANCING EARTH AND SPACE SCIENCE

Tectonics

RESEARCH ARTICLE
10.1029/2020TC006391

Key Points:
- Crustal seismicity reveals a right-lateral duplex as the continental-scale fault setting between 44°00′ and 45°30′ in the Southern Volcanic Zone (SVZ)
- Stratovolcanoes are located in a local transtensional environment inside the duplex
- Seismicity is consistent with documented brittle and ductile deformation, suggesting a continuous shear zone deeper than the brittle crust

Supporting Information:
- Supporting Information S1
- Data Set S1

Correspondence to:
N. Pérez-Estay,
nnperez@uc.cl

Citation:
Pérez-Estay, N., Yáñez, G., Crempien, J., Roquer, T., Cembrano, J., Valdenegro, P., et al. (2020). Seismicity in a transpressional volcanic arc: The Liquiñe-Ofqui fault system in the Puyuhuapi area, Southern Andes, Chile (44°S). *Tectonics*, *39*, e2020TC006391. https://doi.org/10.1029/2020TC006391

Received 18 JUN 2020
Accepted 20 OCT 2020
Accepted article online 23 OCT 2020

Seismicity in a Transpressional Volcanic Arc: The Liquiñe-Ofqui Fault System in the Puyuhuapi Area, Southern Andes, Chile (44°S)

Nicolás Pérez-Estay[1], Gonzalo Yáñez[2], Jorge Crempien[1,2], Tomás Roquer[1,2], José Cembrano[1,2], Pablo Valdenegro[1], Diego Aravena[1], Gloria Arancibia[1,2], and Diego Morata[1,3]

[1]Andean Geothermal Center of Excellence (CEGA–FONDAP), Universidad de Chile, Santiago, Chile, [2]Departamento de Ingeniería Estructural y Geotecnia, Pontificia Universidad Católica de Chile, Santiago, Chile, [3]Departamento de Geología, FCFM, Universidad de Chile, Santiago, Chile

Abstract Understanding the relationship between crustal faults and volcanic activity in transpressional environments is a main goal in geosciences and could help to understand geothermal resources and evaluate geological hazards. In the Andean Southern Volcanic Zone (SVZ), Chile, recorded seismicity is scarce, and few studies have evaluated the relationship between volcanic activity and crustal faults from seismic observations. Thus, in this study, we deployed a seismic network for almost 1 year to understand the brittle deformation of the upper crust within the Puyuhuapi area, located at ~44°S in the SVZ. We analyzed the location and kinematics of seismicity together with previously published field structural geological data. Considering these results, we developed an integrative tectonic model for the area and discussed which faults facilitate magma transport through the crust. Our results indicate the existence of two NNE-oriented seismogenic dextral to dextral-reverse regional faults that generate a duplex in a continental-scale fault setting. Inside the duplex, we observed normal to strike-slip normal focal mechanisms which recurrently have NE trending nodal planes. At a regional scale, a strike-slip tectonic environment has a N60°E/18° shortening direction and a N151°E/03° extension direction. We conclude that stratovolcanoes are located inside the duplex in a local transtensional environment where NE oriented normal faulting may occur. These faults facilitate magma transport since they represent the preferential orientation for dilatational fractures. Conversely, in local transpressional environments such as the Puyuhuapi fault (NNE oriented dextral to dextral-reverse kinematics), only minor eruptive centers of small volume are emplaced, suggesting a less productive magma transportation process.

1. Introduction

Active geological faults represent mechanical weaknesses within the crust, which can trigger and/or promote the further development of fractures during a seismic cycle (e.g., Mogi, 1967; Scholz, 2002). These fractures result in new domains with high permeability, thus generating ideal conditions to promote fluid migration (e.g., Ingebritsen & Gleeson, 2017; Lamur et al., 2017; Pérez-Flores et al., 2017). Consequently, the relationship between crustal faults and fluid migration through the crust has been studied extensively (e.g., Cox, 2005; Faulkner et al., 2010; Gudmundsson, 2011). In particular, along magmatic arcs, crustal faults play a key role in volcanic emplacement, regardless of the local tectonic setting. Some illustrative examples of this link between faults and volcanoes are the Taupo Volcanic Zone in New Zealand (e.g., Cole, 1990; Rowland & Sibson, 2004), the Central American arc (e.g., Corti et al., 2005; LaFemina et al., 2002, 2004), and the Southern Volcanic Zone (SVZ) in Chile (e.g., Cembrano & Lara, 2009; Pérez-Flores et al., 2016). In this paper, we focus on the SVZ, a transpressional volcanic arc where several tectonic models have been proposed to explain the emplacement of volcanoes (Cembrano & Lara, 2009; López-Escobar et al., 1995; Melnick et al., 2006; Nakamura, 1977; Pérez-Flores et al., 2016; Sánchez et al., 2013). However, most of the data supporting these models were obtained between 38°S and 42°S and therefore cannot account for continental-scale variability of the nature, geometry, and kinematics of different fault systems along the whole SVZ (e.g., horsetail fault termination at ~38°S, one main NNE oriented strike-slip fault between 42° and 43°S, and a transpressional duplex between 44° and 46°S). Furthermore, the use of seismic events as a short-term testing methodology for these models remains

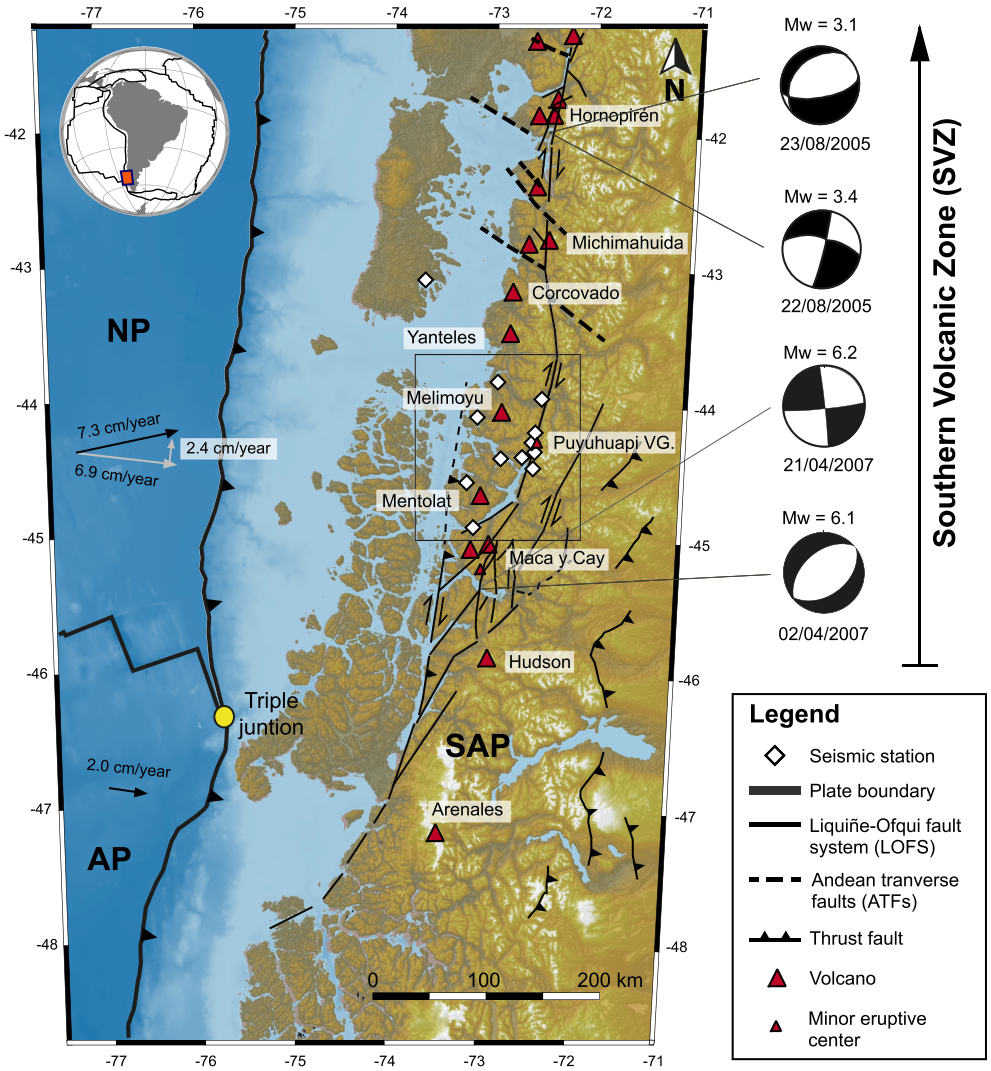

Figure 1. Geomorphological map of the study area. Faults are compiled from Arancibia et al. (1999), Cembrano and Lara (2009), Thomson (2002), and Vargas et al. (2013). Focal mechanisms were obtained from Lange et al. (2008) and Legrand et al. (2011); convergence velocity vectors were obtained from the MORVEL model (DeMets et al., 2010). NP: Nazca Plate. AP: Antarctic Plate. SAP: South American Plate. The Nazca Plate vector was decomposed, in convergence parallel and perpendicular to margin, as shown by the gray arrow. The black rectangle show the specific study area.

largely undeveloped for the SVZ, with some exceptions (Lange et al., 2008; Sielfeld et al., 2019). Hence, further efforts and hypothesis testing must be performed to understand which tectonic model can explain the emplacement of volcanoes in transpressional tectonic environment such as the SVZ.

The SVZ (Figure 1) is a volcanic arc dominated by a transpressional stress throughout a length of ~1,000 km along the Andes, where the Nazca Plate subducts below the South American Plate (López-Escobar et al., 1993, 1995). This volcanic arc has been correlated with the Liquiñe-Ofqui fault system (LOFS) and the Andean Transverse Faults (ATFs) (e.g., Pérez-Flores et al., 2016; Sielfeld et al., 2019). Different authors recognize the important tectonomagmatic role of NS oriented strike-slip faults (master faults) with secondary NE and NW oriented faults of the LOFS (Cembrano & Lara, 2009; Iturrieta et al., 2017; López-Escobar et al., 1995; Melnick et al., 2006; Nakamura, 1977; Pérez-Flores et al., 2016; Sánchez et al., 2013). These authors note that NE oriented strike-slip faults favor the rapid ascent of magma from the asthenosphere due to the orientation of the principal stress axis in this volcanic arc (i.e., a ~N60°E trending direction; Cembrano & Lara, 2009, and reference therein). This occurrence generates NE-aligned flank volcanoes, NE oriented chains of

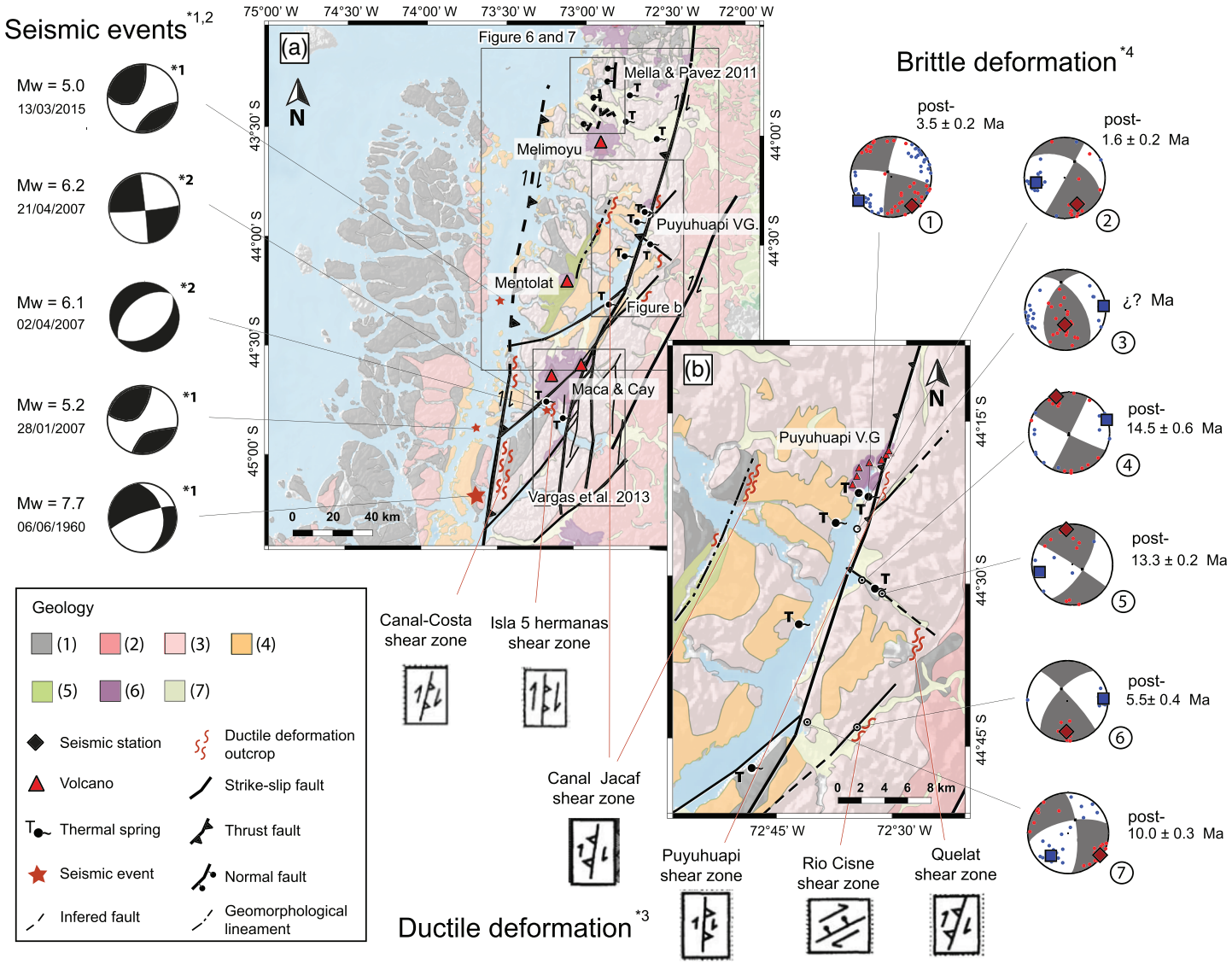

Figure 2. Local structural geology of the study area. (a) Regional map. (b) Local map of Puyuhuapi fjord. Focal mechanisms were obtained from *1Kanamori and Rivera (2017) and *2Legrand et al. (2011). Ductile deformation is according to *3Cembrano et al. (2002). Brittle deformation was obtained from the data of *4Arancibia et al. (1999). Each brittle-structural site is numbered according to Arancibia et al. (1999), and the age of each site was obtained from the same work. Red and blue dots of brittle deformation represent the T-extensional and P-shortening direction of fault planes. Red diamonds and blue squares represent the main extensional and shortening directions, respectively, that were obtained from the statistical Bingham distribution in the FaultKin software (Allmendinger et al., 2012; Marrett & Allmendinger, 1990). The large black square in (a) indicates the study area. Faults and lineaments were obtained from Arancibia et al. (1999), Cembrano et al. (2002), Mella and Páez (2011), SERNAGEOMIN (2003), and Vargas et al. (2013). Part of the map is simplified from Vargas et al. (2013). The geological legend is as follows: (1) Paleozoic metamorphic basement; (2) Paleogene and cretaceous intrusive rocks; (3) Miocene intrusive rocks; (4) Eocene-to-Miocene marine volcano-sedimentary rocks (Traiguen formation); (5) Traiguen formation with low-grade metamorphism; (6) Quaternary volcanic rocks; and (7) Quaternary sedimentary deposits.

stratovolcanoes, and NE elongated clusters of monogenetic cones (Cembrano & Lara, 2009; López-Escobar et al., 1995; Nakamura, 1977). The present study focuses on the southern tip of the SVZ, in the Puyuhuapi area, where a continental-scale strike-slip duplex has been documented (Cembrano et al., 1996) as shown in Figures 1 and 2. In this area, the link between volcanoes and tectonics has been analyzed only with elastoplastic modeling. The results of previous studies suggest that the intersection between NS and NE oriented faults may serve as a long-lived magma pathway (Iturrieta et al., 2017).

The purpose of this work is to test the existing tectonic models using a novel crustal earthquake catalog, in order to improve the understanding of the relationship between volcanoes and crustal faults in

transpressional environments. If the interaction between crustal fault systems and hot fluid circulation can be understood in the study area, the nature and spatial configuration of geothermal reservoirs and geological hazards will be better constrained. Specifically, we selected a small study area (80 × 80 km) near the town of Puyuhuapi (Figures 1 and 2), which contains two active stratovolcanoes, nine minor eruptive centers, and nine hot springs, all of which are spatially related to map traces of the LOFS. We recorded the seismicity in this area for ~1 year in an attempt to constrain the current deformation state of the crust. By coupling seismic observations with previous studies of the structural geology along exhumed faults, we define the deformation process over time, which in turn allows us to define the main active crustal faults and their kinematics. Finally, we propose a tectonic model to explain the relationship between different types of volcanoes (i.e., minor eruptive centers or stratovolcanoes) and different kinds of faults and provide a comparison between the model and previous models for the SVZ.

2. Tectonic Background

The tectonic of the SVZ (33–49°S) is dominated by the oblique subduction of the Nazca Plate beneath the South American Plate, which has a N76°E trending convergence velocity vector and a convergence rate of ~73 mm/yr (DeMets et al., 2010). The direction of the convergence is presumed to have been largely stable since the Miocene (Pardo-Casas & Molnar, 1987); however, the convergence rate has decreased from 19 cm/yr to the actual value of 7.3 cm/yr since the Miocene (Quinteros & Sobolev, 2013), as evidenced by exposed brittle faults and ductile shear zones (e.g., Arancibia et al., 1999; Cembrano et al., 2002; Lavenu & Cembrano, 1999). The other first-order tectonic element in the region is the triple-junction which occurs at the Taitao Peninsula, where the Chile Rise subducts beneath the Chile-Peru trench (Figure 1). South of this triple-junction, continental tectonics are controlled by the convergence between the Antarctic and South American plates, which occurs at a rate of 20 mm/yr with a N88°W trending direction (DeMets et al., 2010).

2.1. Crustal Faults of the SVZ

Crustal deformation in the SVZ is accommodated by two groups of faults: the LOFS and the ATF, as shown in Figure 1 (e.g., Cembrano et al., 1996; Cembrano & Lara, 2009; Melnick et al., 2006; Pérez-Flores et al., 2016). The LOFS is an active fault system composed of NS oriented master faults with dextral and dextral-reverse kinematics accompanied by NE to ENE oriented dextral and dextral-normal faults (e.g., Arancibia et al., 1999; Iturrieta et al., 2017; Lange et al., 2008; Lavenu & Cembrano, 1999; Pérez-Flores et al., 2016; Rosenau et al., 2006 ; Villalobos et al., 2020). Geological evidence indicates that the LOFS is a continental-scale shear zone dominated by a transpressional regime, with a NS oriented dextral-slip deformation that partially accommodates the margin-parallel component of the plate-convergence vector (see Figure 1). The ATF includes a group of NW oriented sinistral and sinistral-reverse faults oblique to the current orogen which were apparently inherited from pre-Andean processes (e.g., Pérez-Flores et al., 2016; Radic, 2010; Rosenau et al., 2006). Such faults and morphotectonic lineaments are thought to be related to the tectonic segmentation of the Andes, Paleozoic-Mesozoic volcanisms, and the formation of NW-WNW trending Mesozoic basins (e.g., Melnick et al., 2009; Radic, 2010; Rivera & Cembrano, 2000). The study area is located in the southernmost termination of the LOFS, where two first-order NNE-oriented faults comprise a strike-slip dextral duplex with at least three second-order NE oriented faults splaying off the LOFS (Cembrano et al., 1996; Iturrieta et al., 2017) (44–46°S).

2.2. Volcanic Features

Many volcanoes in the study area are spatially associated with NS to NE oriented faults (Cembrano & Lara, 2009), whereas in the northern segment of the LOFS, volcanism is locally related to NE and NW oriented transverse faults and fault intersections (e.g., Pérez-Flores et al., 2016).

Evidence of Quaternary volcanism has been provided by tephrochronological analysis of two lakes in the study area, which indicate the Quaternary activity of Mentolat and Melimoyu volcanoes (Stern et al., 2015). Melimoyu volcano (44.08°S/72.88°W; elevation: 2,400 m above sea level, a.s.l.) is a large glacier-covered stratovolcano that is elongated 10 km in an E-W direction, with a small summit crater with a diameter of 1 km. There is no record of historic activity for this volcano, yet tephra fall deposits preserve evidence of two late Holocene explosive eruptions less than 3,000 years ago (Naranjo & Stern, 2004). The volcano is mainly

andesitic; however, proximal tephra deposits from recent eruptions grade from dacitic pumice upward to coarse dark basaltic scoria (López-Escobar et al., 1993; Naranjo & Stern, 2004). Meanwhile, Mentolat volcano (44.70°S/73.10°W; elevation: 1,660 m a.s.l.) is a stratovolcano formed of Pleistocene to Holocene basaltic andesites and andesite lava flows (López-Escobar et al., 1993). The volcano is capped by a large summit crater infilled with either a Holocene dome or simply ice. Mella et al. (2012) reported two major eruptions less than 4,000 years ago and some local reports suggest that an eruption occurred in the early eighteenth century.

Additionally, close to the seismic network, there are other minor eruptive centers with observed postglacial activity (Lahsen et al., 1994), which are referred to as the Puyuhuapi Volcanic Group (PVG) (Figure 1). These centers consist of pyroclastic cones and basaltic lava flows (Lahsen et al., 1994) and are spatially associated with one of the NS trending master faults of the LOFS (Figure 1).

2.3. Regional Seismicity

The availability of seismic data for the study area is limited, mainly due to the lack of long-term local seismic networks. However, in 2007, a large seismic swarm related to the LOFS was recorded to the south of the study area (Agurto et al., 2012; Legrand et al., 2011; Mora et al., 2010; Russo et al., 2011; Vargas et al., 2013). The most relevant features of this seismic sequence were as follows: (i) a high b value of 2.59 ± 0.3, which suggests fluid circulation close to the Macá and Cay volcanoes (Legrand et al., 2011); (ii) a strike-slip focal mechanism of the main event (M_w 6.2), with the most probable solution being a NNE oriented dextral fault accompanied by another event (M_w 6.1) produced by a NE-oriented normal fault (Agurto et al., 2012; Legrand et al., 2011; Russo et al., 2011), which implies a present-day activation of the principal and secondary LOFS faults (Figure 1); and (iii) the depth of the events was within the upper 10 km of the crust (Agurto et al., 2012; Legrand et al., 2011; Mora et al., 2010), suggesting a shallow brittle-plastic transition in this region.

Kanamori and Rivera (2017) analyzed a crustal earthquake which occurred on 6 June 1960 as an aftershock of the 22 May 1960 M_w 9.5 Great Chilean Earthquake. This crustal earthquake ($M_w = 7.7$) has five possible focal mechanisms, all of which have a ~N10°W striking nodal plane and four of which show primarily strike-slip kinematics (Figure 2 shows one of the possible focal mechanisms and Figure S10 shows all of the possible focal mechanisms). Two other earthquakes with similar focal mechanisms were recorded by the Global Centroid Moment Tensor catalog in the last century (Kanamori & Rivera, 2017), as also shown in Figure 2.

2.4. Local Structural Geology

Both brittle and ductile deformation have been recorded in the study area (Arancibia et al., 1999; Cembrano et al., 2002; Lavenu & Cembrano, 1999; Mella & Páez, 2011). Each of these styles of deformation is extremely important for the interpretation and discussion presented in this study—brittle deformation for understanding similarities and differences between long-term (structural geology) and short-term (seismicity) deformation processes, and ductile deformation to compare the deformation at deeper structural levels which are now exhumed. By combining these data, we assessed the temporal evolution of the prevailing deformation processes and kinematics in the study area since at least ~4 Ma (considering the deformation dated in Cembrano et al. 2002).

Brittle deformation in the study area has been explained by two temporally separated stress regimes identified from fault-slip analyses: (1) a post-Miocene regime with an EW shortening direction; and (2) a Quaternary regime with a ~N60°E shortening direction (Arancibia et al., 1999; Lavenu & Cembrano, 1999). Outcrops which show evidence of brittle deformation are shown in Figure 2, with fault planes observed on granodiorites and diorites (obtained from Arancibia et al., 1999). Brittle deformation is younger than the biotite or hornblende $^{40}Ar/^{39}Ar$ ages of hosting rocks summarized in Figure 2. Additionally, north of Melimoyu volcano, NE oriented faults with lengths of ~2–5 km accompanied by NS oriented normal faults with lengths of 5–20 km have been mapped crosscutting Miocene to Pliocene intrusive rocks (Mella & Páez, 2011; see upper part of Figure 2a).

On the other hand, the kinematics of ductile deformation have been defined from the lineation and foliation measured in mylonitic rocks (Cembrano et al., 2002). Most of the ductile deformation in the study area can

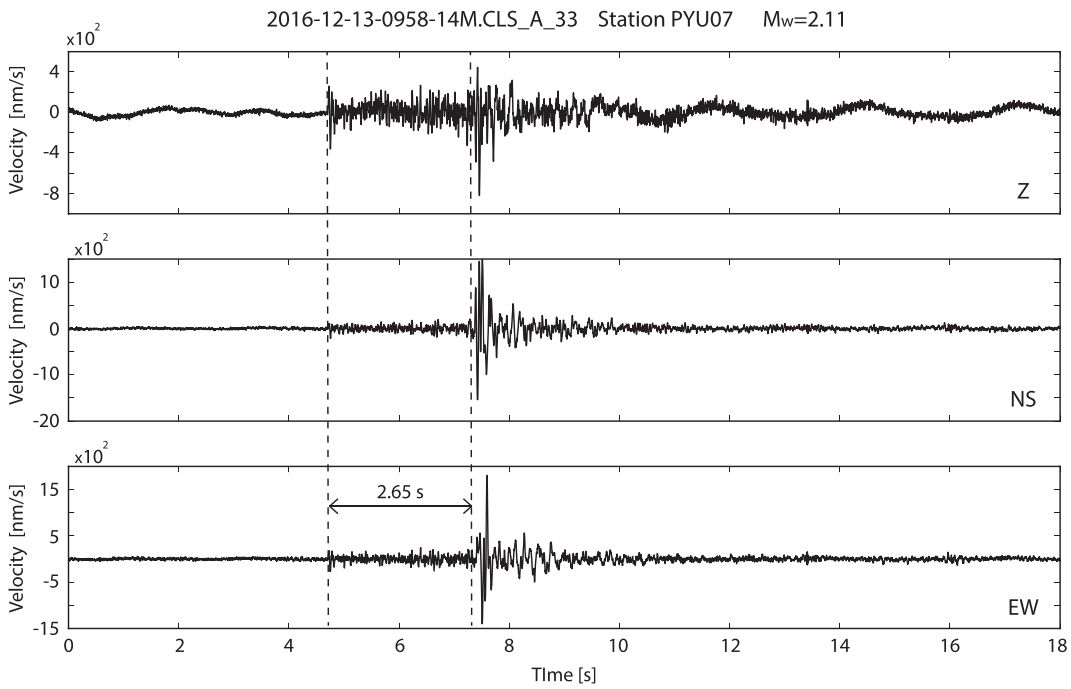

Figure 3. Example of the waveform of a "class A" crustal event with a magnitude of $M_w = 2.1$ (13 December 2016, 09:58 UTC) recorded at station PYU07. Three components are shown, namely vertical (Z) and horizontal (NS and EW). The arrivals of *P* and *S* waves are clearly observable in the Z and EW components, respectively. The small difference between the arrival times of the *P* and *S* waves indicates a short distance between the source and receiver (which for this particular case is estimated to be ~22 km); this was confirmed by the location process (which defined a source-receiver distance of 21 km). Note that all the events analyzed in this work had $M_w > 2$, as only events of these sizes were detected at a minimum of six stations.

be explained in terms of right-lateral to right-lateral-reverse kinematics (Figure 2). A specific outcrop, named the Rio Cisnes shear zone, shows ~N60°E normal right-lateral kinematics. Ductile deformation has been dated at 4–6 Ma based on biotite, hornblende, and muscovite $^{40}Ar/^{39}Ar$ ages from mylonitic rocks (Cembrano et al., 2002).

3. Methods

3.1. Seismic Data

We deployed a seismic network consisting of six S31f-2.0a borehole seismometers (IESE, Auckland, New Zealand; three-component, short period, natural frequency of 2 Hz; locations shown in Figure 1). The sampling rate was set to 500 samples per second. The seismic network collected data for 10 months between August 2016 and May 2017. To improve the spatial resolution of the network, we included data recorded by five permanent stations (Guralp 6TD, Guralp Systems, Reading, UK; three-component broadband seismometers) belonging to the Volcanic Observatory of the Southern Andes (OVDAS) and by one station belonging to the National Seismological Center of Chile (CSN). The data from the OVDAS and CSN stations were recorded at 100 and 40 samples per second, respectively. The continuous seismograms were visually inspected to identify crustal earthquake events. We only considered events with less than 8 s between the arrival times of the *P* and *S* waves; thus, limiting the considered seismic activity to distances of less than ~65 km from the network. We detected 272 seismic events, which were classified into two types: (i) Class A events, which were clearly detected by at least six stations—that is, event which have more than 12 observed arrivals of *P* and/or *S* waves—and (ii) Class B events, with more than seven clear *P* and/or *S* wave. According to this classification, we obtained 117 Class A events and 155 Class B events. Figure 3 shows velocity seismograms of a Class A event recorded at station PYU07.

3.2. Earthquake Location

We manually carried out the precise determination of the arrival times of *P* and *S* waves on the recorded seismograms using the SEISAN software (Ottermöller et al., 2014). To obtain an initial estimate of the location of the events, we used the Hypocenter software (Lienert, 1994), which requires a precise local velocity model. To determine the most suitable model, we located events using different seismic velocity models and evaluated which one had the smallest arrival-time error using the methodology described below.

First, using the Wadati software of the SEISAN package, we defined a Vp/Vs ratio of 1.72 for Class A and Class B events. Then, as a first iteration, Class A events were located using 25,000 different velocity models in the range defined and depicted in Figure 4a, which contains the range of velocities of all the velocity models observed worldwide (Mooney et al., 2002). Then, from these results, we chose 500 models with the smallest root-mean-square (RMS) time errors to define a new velocity range (the second iteration in Figure 4a). From the range defined as the second iteration, we computed 125,000 different models with better stratification and a higher velocity resolution (layer thickness 0.5–1 km, velocity resolution 0.1 km/s) and chose the model with the smallest RMS error. Thus, our method involves searching for the best velocity model from the entire space of possibilities via a grid-search technique and is not an optimization or inversion technique as is provided by other available software (e.g., Velest).

We applied this method to Class A events only as they represent robust data with a lower chance of having uncontrolled local variability. Most of the earthquakes were located within the upper 15 km of the crust; hence, the velocity model was well constrained within this depth range (see Figure 4a).

To obtain accurate earthquake locations, we relocated Class A events using the HypoDD software (Waldhauser, 2001; Waldhauser & Ellsworth, 2000). To ensure that the distance between events was small with respect to the station-event distance, we relocated event pairs that were separated by less than 5 km. In order to obtain more equations than the number of degrees of freedom for each event pair, we only used event pairs for which a minimum of eight phase observations were available. Isolated events without pairs within 5 km were not processed with HypoDD (27 of 117 events); however, we retained their hypocentral location. These events were processed using the location-quality filter described in the last paragraph of this subsection and are shown in the supporting information (file with locations: Class_A_locations.txt). Waldhauser (2001) paid careful attention to address the location error estimated with the HypoDD software, and the reliability of the error values must be tested using statistical methodologies (e.g., Waldhauser & Ellsworth, 2000). To test the location error, we used a bootstrap statistical resampling approach similar to that of Waldhauser (2001), eliminating one event per iteration in two cases—namely when the events location start (1) in the center of the cluster or (2) in the *Hypocenter* catalog—totaling 234 (117×2) iterations. The variability of the locations can be observed in Figures 4f and 4g. The 90% confidence level is contained to around 2–3 km, which is sufficient to resolve and separate the main faults in the study area and to draw conclusions regarding the tectonic setting of the region.

Finally, we filtered the 117 Class A hypocenters by their location quality based on the following criteria: (1) location error of less than 3.5 km; (2) RMS error of less than 0.3 s; (3) events with more than 12 clearly identified *P* and/or *S* wave phases; and (4) azimuthal gap below 240°. Following this filtering process, a total of 81 events remained, which will be considered throughout the rest of this paper. The mean location error was 1.2 km in both the horizontal and vertical directions, and the mean RMS was 0.13 s. Figures 4b–4e presents the statistics for the locations of the 81 remaining events. Further analysis of the earthquake location reliability in terms of the event hypocenters and the network distribution is presented in section 4.

3.3. Earthquake Focal Mechanisms and Magnitudes

To calculate focal mechanisms, we considered events with at least nine clear *P* wave polarities, RMS values of less than 0.25 s, and an azimuthal gap of less than 180°. We constrained focal mechanisms using the FOCMEC, HASH, and FPFIT softwares from the SEISAN package. The FOCMEC focal mechanism solutions were calculated with no polarity error to provide a range of possible solutions. Then, we calculated the solutions with HASH (allowing one polarity error) and FPFIT. Lastly, we chose the solution which provided the best fit to all possible FOCMEC solutions using our own Python code (explained in detail in Text S4). A summary of the focal mechanism selection process is presented in Text S4 and Figures S9 and S10; meanwhile, the statistical details of the selected mechanisms can be found in Table S2. To quantify

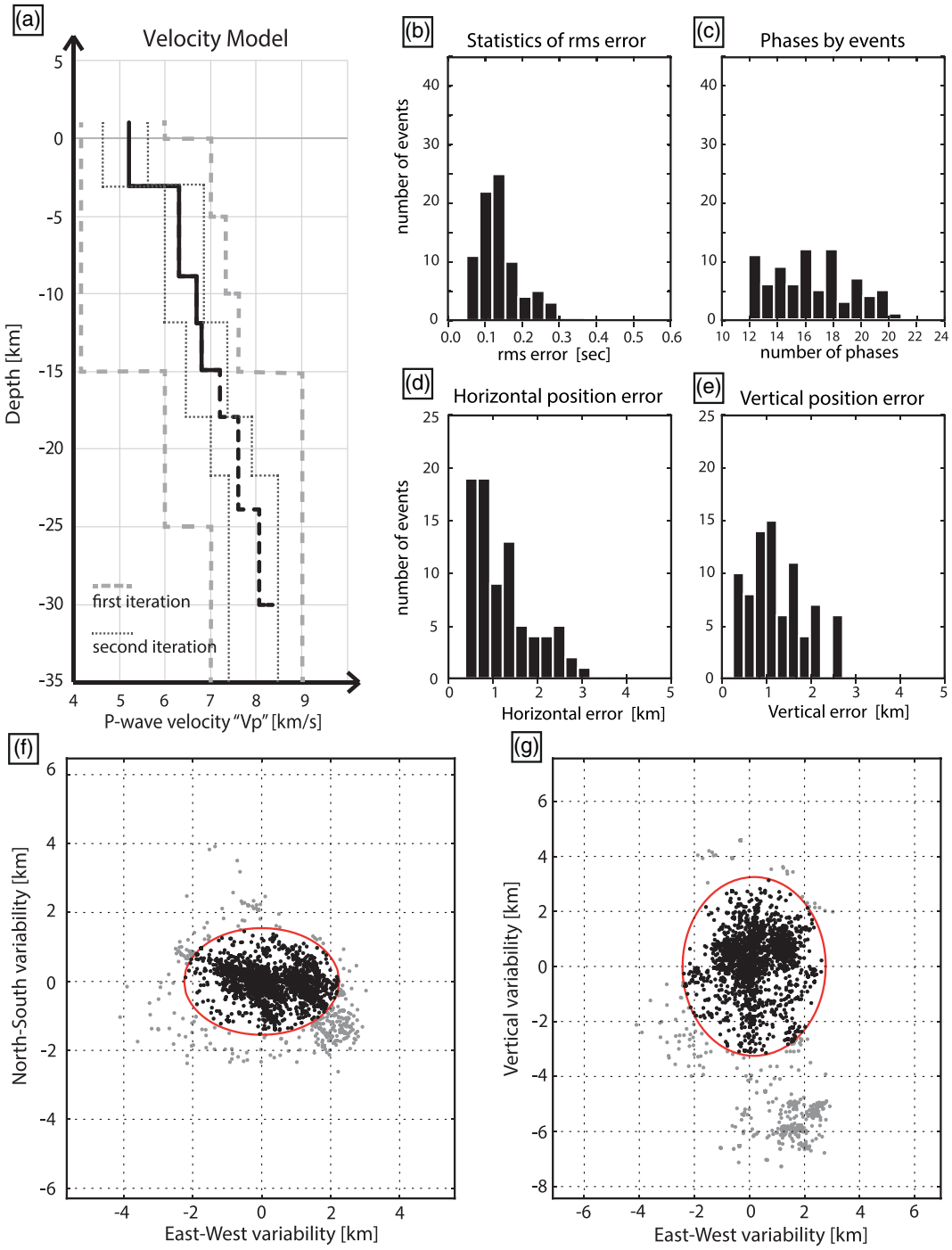

Figure 4. The velocity model used to obtain earthquake locations, and the event localization statistics. (a) Gray lines show the range of the first and second iterations to find the best velocity model. The best velocity model is shown by the solid black line. Most of the earthquakes are located within the upper 15 km of the crust, and the refracted rays in layers below 15 km represent only 3% of the detected rays (53 of 1,820 raypaths); thus, velocity layers below 15 km are poorly resolved; these are shown by dashed black lines. Panels (b)–(e) show statistics for the 81 events that passed the location-quality filtering using the following criteria: (1) location error below 3.5 km; (2) number of phases greater than or equal to 12; (3) root-mean-square (RMS) value of less than 0.3 s; and (4) azimuthal gap below 240°. Panels (f) and (g) show the variability of the locations obtained using the HypoDD software, calculated using a bootstrap analysis similar to that of Waldhauser and Ellsworth (2000). Both horizontal and vertical directions were analyzed. The red ellipses contain 90% of the events.

the uncertainty of the mechanisms, we calculated the RMS error of the *P* and *T* directions of each mechanism using 90% of the possible focal mechanisms defined by the FOCMEC software (each uncertainty calculation is shown in the supporting information "Focal_mechanisms_uncertenty.rar"). We chose 90% to avoid giving weight to a few outlier solutions; however, the supporting information contains the RMS of the *P* and *T* directions for 100% of the FOCMEC solutions as well as a detailed analysis of the uncertainty of the trend and plunge of the *P* and *T* directions, separately.

Additionally, in three cases, nearby events were unified to obtain a unique focal mechanism solution (referred to in this article as composite mechanisms). This methodology allowed us to increase the number of *P* wave polarities and therefore obtain better statistics. This method assumes (although it is not necessarily true) that most of the events share the same focal mechanism solution, or at least, all of the *P* wave polarities are together representative of the main focal mechanism. This is likely to be true for the composite mechanism presented in this work, since the events selected to calculate a composite mechanism are closer than 2 km from each other and occur within a time window of 1–5 days; therefore, these probably represent the tectonic response of a single deformation tensor. In fact, the same assumption is followed to characterize a fault from a given structural-geology outcrop, since many fault outcrops represent several striking and dipping striated surfaces of cm^2 to tens of m^2 with common deformation axes, rather than a single fault plane (Petit, 1987). Although more than one fault can be activated within a radius of 2 km around the selected events, as well as a single fault, fault intersections probably have coherent deformation axes (Kim et al., 2004). Hence, our composed mechanisms are an observation of the mean deformation process around some specific earthquake clusters.

An important tectonic issue is defining the faulting type of focal mechanisms and the tectonic regime of an area. To determine the faulting type of focal mechanisms objectively, we employed Kaverina et al.'s plot classification (Kaverina et al., 1996) using the FMC open source software (Alvarez-Gomez, 2019). This classification depends on the plunge of the *P*, *T*, and *B* axis of each focal mechanism and allows the faulting type to be described as normal, reverse, strike-slip, or a mixture between them—either normal strike-slip or strike-slip normal depending on the predominant displacement component. This classification is shown later in results section 5 (specifically in Figure 7c). Equally importantly, to analyze the tectonic regime of the study area, we observed the *P* and *T* directions of seismic events and structural geological data (from Arancibia et al., 1999) in a Schmitdt spherical projection; and calculated the main shortening and extension directions based on the statistical Bingham distribution in the FaultKin software (Allmendinger et al., 2012; Marrett & Allmendinger, 1990). Additionally, we calculated the strain ellipsoid shape ratio ($R = (E_2 - E_3)/(E_1 - E_3)$), where E_1, E_2, and E_3 are the eigenvalues of the Bingham moment tensor, or the *T*, *B*, and *P* axes, respectively (e.g., Diraison et al., 2000; Pérez-Flores et al., 2016). Values of *R* between 0.65 and 1 indicate flattening deformation; values between 0.35 and 0.65 indicate plane-strain deformation; and values between 0 and 0.35 indicate constrictional deformation (Diraison et al., 2000). These three deformation styles correspond to transpressional, strike-slip, and transtensional deformation states, respectively (Dewey et al., 1998).

The above methodology has been widely used to analyze fault slip data (e.g., Diraison et al., 2000; Giambiagi et al., 2017; Pérez-Flores et al., 2016) but has not commonly been used to analyze focal mechanisms. However, the strike/slip/rake data of double-couple focal mechanisms could be used as a substitute for fault slip data obtained from the field, since both can be used to calculate the principal strain axes (Allmendinger et al., 2012). Some examples of using double-couple focal mechanisms and fault slip data in the same terms are Obstubo et al. (2008)—who used both plane solutions from focal mechanisms to calculate the stress tensor using MIM (a fault-slip data method of Yamaji, 2000)—and Michael (1984, 1987), who developed the same methodology for focal mechanisms and fault slip data in order to calculate the stress tensor. In the present study, we chose to compare the fault-slip data and focal mechanisms in terms of strain instead of stress, since transtension and transpression have been defined as a deformation process, not a stress process (Dewey et al., 1998; Harland, 1971). Additionally, using the Bingham distribution for the calculation of regional *P* and *T* directions, we avoid the ambiguity of selecting one of the FM plane solutions since the *P* and *T* directions are equal for both FM-solutions. This approach allows an internally consistent comparison to be made between fault-slip data and seismological data by using the same mathematical principles.

For each of the 81 selected events, we calculated the seismic moment magnitude based on the displacement spectra. To calculate the displacement spectra, we used a 2.5 s time window starting from 0.5 s before the *P*

wave arrival for all the traces of each station. We repeated the same process for S waves. Then, we calculated the seismic moment (M_0) according to the flat segment of the displacement spectra (e.g., Havskov & Ottemöller, 2010) and the moment magnitude (M_w) by applying the Kanamori formula (Hanks & Kanamori, 1979). The moment magnitude presented in this work is the mean of all traces and all stations (for details of the moment magnitude calculation, see Text S3 and Figure S8 in the supporting information).

4. Reliability of Locations and Focal Mechanisms

Generally, theoretical location errors are restricted to 3 km in the vertical and horizontal directions (see Figures 4d and 4e); this is in agreement with the results of the bootstrap analysis performed in this study, where 90% of the earthquakes location uncertainties are enclosed within an ellipsoid with a horizontal diameter of ~2.5 km and a vertical diameter of ~3 km (Figures 4f and 4g). However, our seismic network does not have an ideal spatial distribution as the region has limited access due to the presence of fjords, islands, rough topography, dense forest, and the presence of few onshore areas that are highly exposed to sea level fluctuations, hampering the deployment of seismic stations. Thus, these results need to be interpreted with caution; nevertheless, we are convinced that they provide reliable and geologically consistent information. To understand and quantify the uncertainty of the location results, in Figure 5 we plot the azimuthal gap, the nearest-station distance and the amount of stations that recorded the earthquakes, for different longitudes. We chose to separate the results by longitude since the major spatial bias is related to the poor coverage of seismic stations in the western side of the study area. The events were grouped into four areas according to their longitude location (Figure 5a).

Location errors due to the number of stations and the azimuthal gap were analyzed statistically by Bai et al. (2006). They concluded that 15 stations and an azimuthal gap of 210° lead to a location error (vertical and horizontal) smaller than 1 km. This error was stable regardless of whether the number of stations increased or the station distributions was improved. However, the same study showed that, even considering our worst-covered event, location errors do not considerably increase; indeed, according to Bai et al. (2006), events which are recorded on six stations have locations errors restricted to 1.5 km in the vertical and horizontal directions, and events with an azimuthal gap of 240° have errors of ~1 km in both directions. Additionally, the influence of the nearest-station distance on location uncertainties has been investigated using well-known events such as explosions and local earthquakes, with researchers concluding that it is necessary to have at least one station closer than 30 km from the epicenter (Bondár et al., 2004; Dewey et al., 1999). Other authors advise a rule of thumb in which a reliable event is required to be measured by more than one station within a distance equal to two focal depths (Havskov & Ottemöller, 2010). In the present study, this rule of thumb implies distances between 10 and 20 km, depending on the specific event.

According to our longitudinal analyses (Figure 5), the middle and eastern areas satisfy the requirements for the azimuthal gap and nearest-station distance, and the events located in these areas always have more than six stations recording P and S phases. In contrast, the western and easternmost areas do not satisfy the requirements for the azimuthal gap and nearest-station distance; however, the events within these areas always have more than seven recording stations (Figures 5f–5h). Considering this analysis, geological interpretations of the western and easternmost areas are questionable; meanwhile, the middle and eastern areas present reliable location errors, which allow more reliable tectonic interpretations.

However, we decided to keep the western events, despite their inherent location inaccuracies, as they represent an important number of crustal earthquakes (Figure 5d), with the largest seismic energy release in the region for the studied time window (Figure 5c). Thus, these events provide valuable information to determine the nature of brittle deformation in this whole tectonic segment. Consequently, the western events were only used to contextualize the regional seismic behavior shown in Figure 6; however, they were not used to infer precise fault-zone details (e.g., the striking and dipping attitude of faults).

Uncertainties in the focal mechanisms were quantified from the variability of the P and T directions. We include these uncertainties in Figure 7a and Table S2, where all focal mechanism statistics can be found, as well as in the supporting information "Focal mechanisms uncertainty", which presents a detailed analysis of the uncertainties in the trend and plunge of the P and T directions for each focal mechanism. The uncertainty is summarized in Figure 5b, in which focal mechanisms are grouped in the same four longitudinal domains as in the previous analysis. Similar to the locations, the uncertainty in the focal mechanisms has

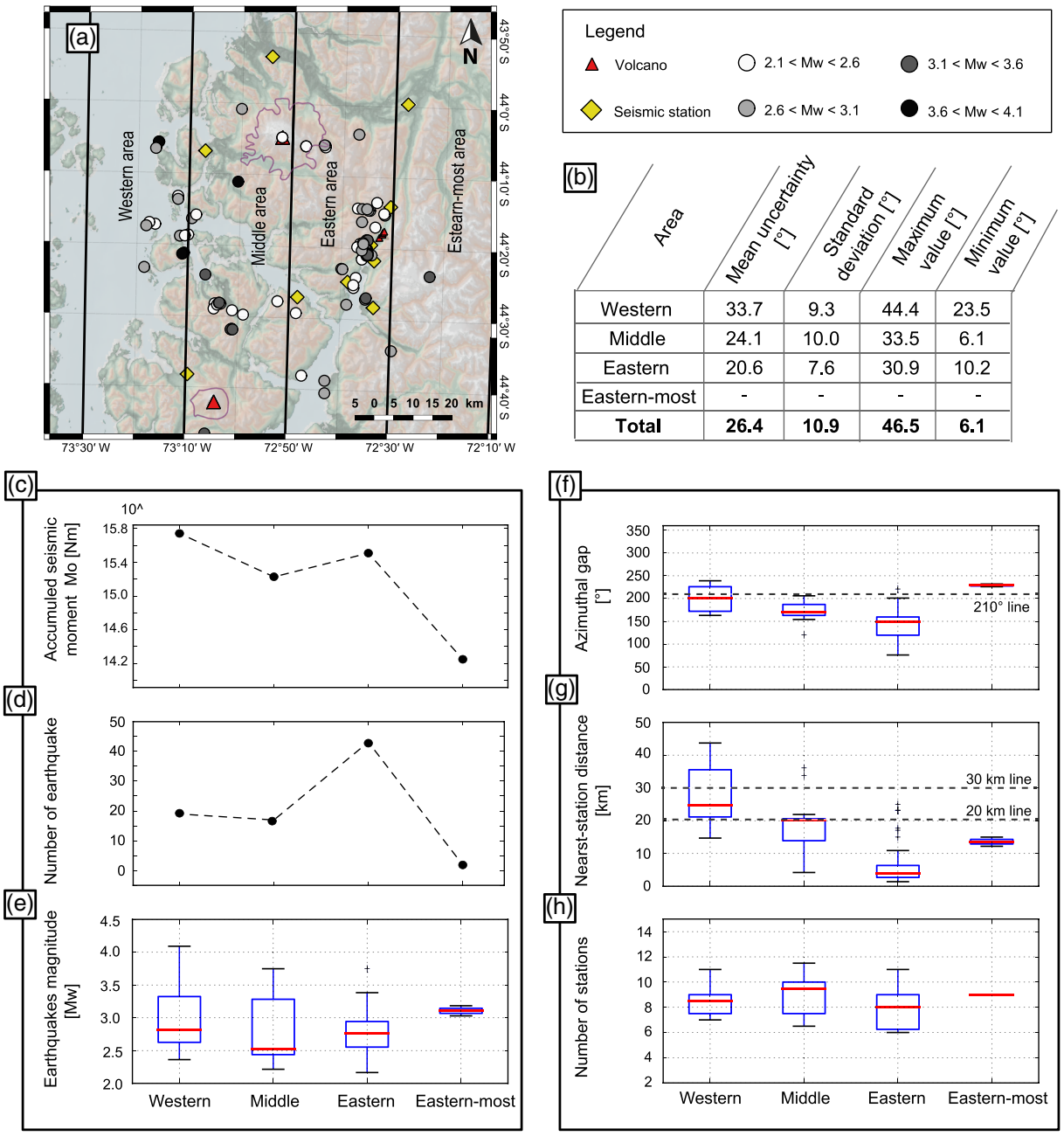

Area	Mean uncertainty [°]	Standard deviation [°]	Maximum value [°]	Minimum value [°]
Western	33.7	9.3	44.4	23.5
Middle	24.1	10.0	33.5	6.1
Eastern	20.6	7.6	30.9	10.2
Eastern-most	-	-	-	-
Total	**26.4**	**10.9**	**46.5**	**6.1**

Figure 5. Longitude analysis of the earthquakes and network parameters. (a) Map showing seismic events and the different areas, which are separated by 20 minutes of degrees, and start with the western stations. (b) Summary of the uncertainties for the focal mechanisms in each area. Values were calculated using the uncertainties of the *P* and *T* directions (these values can be found in Table S2 in the supporting information). Panels (c)–(e) show earthquake statistics for the different areas. Panels (f)–(h) show seismic network statistics related to the location accuracy for the events in different areas. For the 81 selected events, all the recording stations observed the *P* and *S* wave arrivals.

a longitude bias, with focal mechanisms in the western area having the highest uncertainties and those in the eastern and middle areas having an acceptable uncertainty. Additionally, the focal mechanisms in the western area are poorly constrained due to the large hypocentral uncertainties in this area, previously explained. Given these facts, the middle and eastern areas have acceptable uncertainties to be employed for the calculation of the strain regime and kinematic classifications, whereas the same is not true for the western area. Finally, considering the location uncertainty and the mean RMS of the focal mechanisms (33°, 26°, and 20° for western, middle, and eastern area, respectively), the interpretation of the focal

mechanisms allows low-confidence, acceptable-confidence, and high-confidence conclusions to be made regarding the tectonic regime for each area, respectively. To reduce uncertainties, focal mechanisms in the western area (i.e., Events 1, 2, 4, and 5 in Figure 7), and high-RMS mechanisms (i.e., Event 14) were not considered in section 6.

5. Results

5.1. Regional Seismicity

The regional seismicity in the Puyuhuapi area reveals a presently seismogenic and kinematically complex fault system. During the 10-month instrumental deployment period, 81 events were recorded

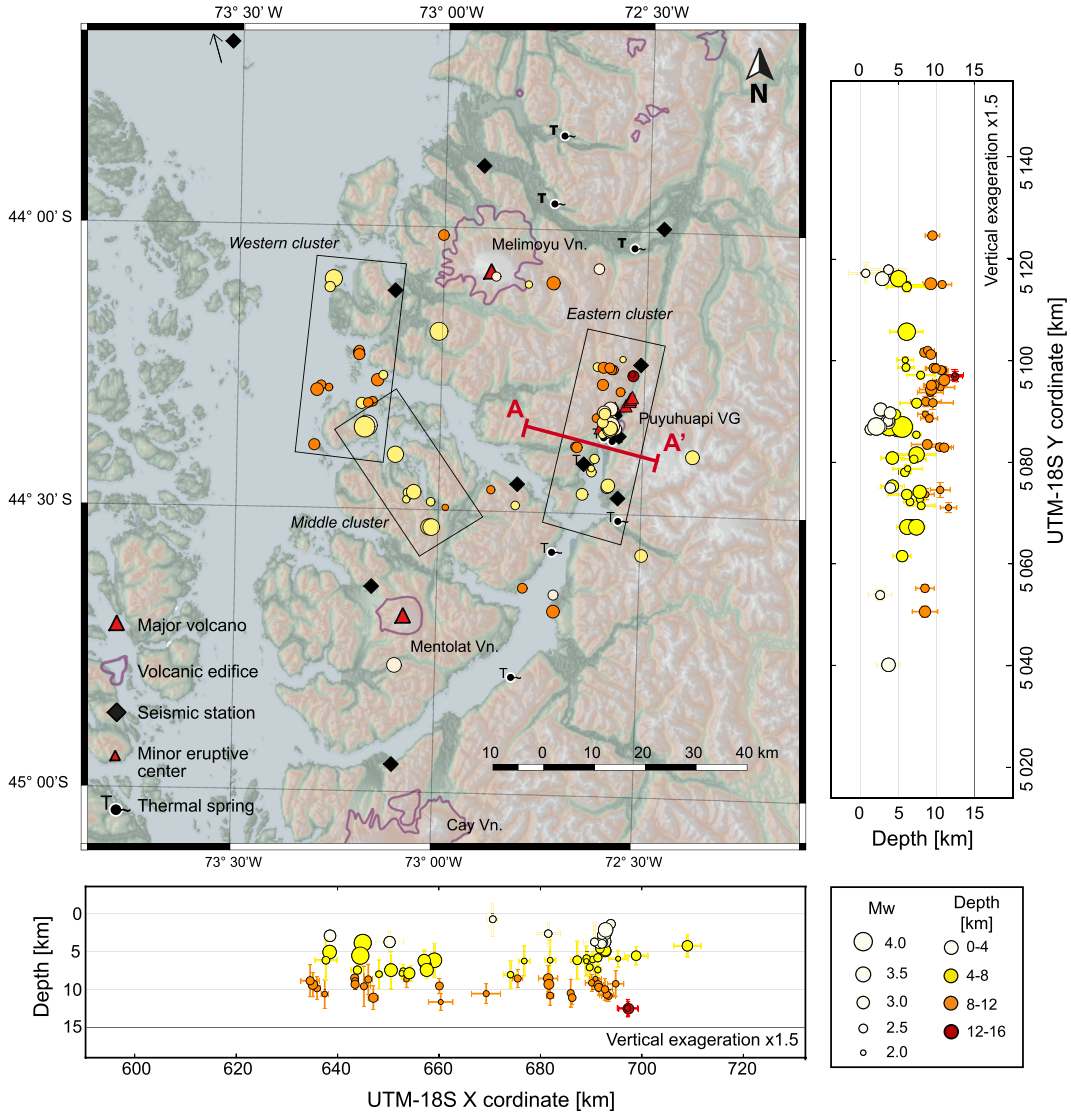

Figure 6. Locations of the 81 selected events after the location-quality filtering (more than 12 arrivals of *P* and/or *S* waves, location error less than 3.5 km, RMS less than 0.3 s, azimuthal gap below 240°). Seismic stations are shown by black diamonds; one station that was located outside of the map area is indicated at the upper edge of the map by arrows representing the direction toward the station location. Profile AA′ is described in Figure 8. Areas with clustered events are marked with black rectangles. The areas selected are also coherent with the spatial distribution of Class A and B events, which is shown in figures S5 and S6 in the supporting information. Latitudinal and longitudinal profiles project the observed seismicity along these orthogonal directions, where error bars represent the uncertainty in locations (in km). Both profiles have a vertical exaggeration of 1.5.

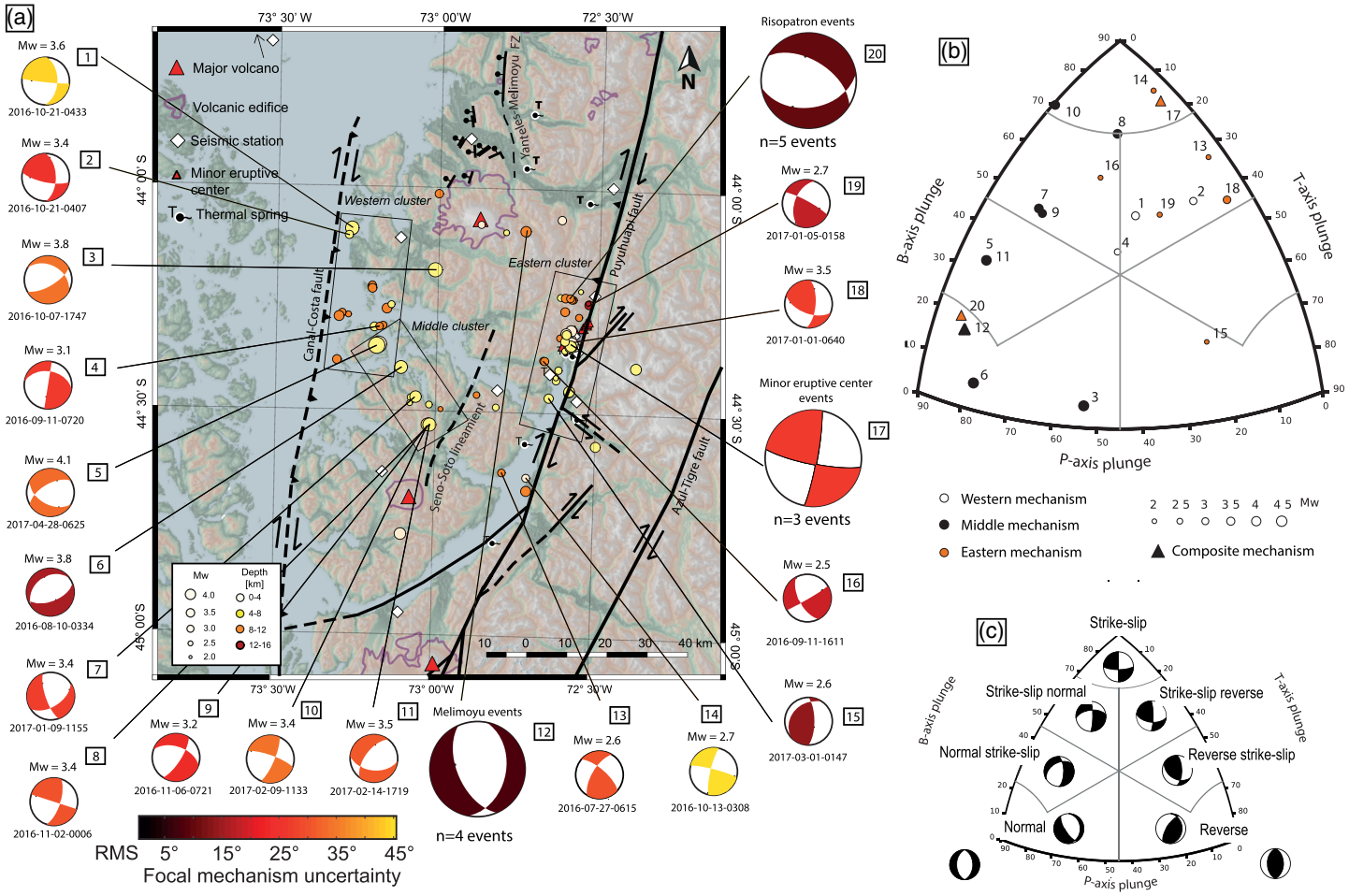

Figure 7. (a) Natural seismicity and corresponding focal mechanisms. In the text, we refer to each focal mechanism by the boxed number displayed next to it. Faults are from Arancibia et al. (1999), Cembrano et al. (2002), Lavenu and Cembrano (1999), Mella and Páez (2011), SERNAGEOMIN (2003), and Thomson (2002). The RMS values of earthquakes were estimated from the average of the *P* and *T* direction variability shown in Table S2 and the supporting information "focal_mechanisms_uncertenties.Rar." The Events 12, 17, and 20 are composite focal mechanism, for details see methodological section 3.3. (b) Kaverina plot of the focal mechanisms, where the number of each mechanism is the same as in (a) (this plot was made using the FMC software of Alvarez-Gomez, 2019). (c) The meaning of each area in the Kaverina plot.

which satisfied the location-quality filtering criteria. The spatial distribution of seismicity was not homogeneous but rather was distributed along geomorphological lineaments generated by fjords, especially the two main NNE-trending fjords (Figure 6). These fjords are a geomorphological expression of the mapped NNE-oriented regional faults of the LOFS (Arancibia et al., 1999; Cembrano et al., 1996, 2002) (see Figure 7). Accordingly, a longitudinal profile shows that most of the seismicity is concentrated in the eastern and western flanks of the study area (see longitudinal profile in Figure 6); however, a latitudinal profile shows a homogeneous spatial distribution in the NS direction. Additionally, most of the recorded seismicity is restricted to the region between the two main NNE oriented regional faults (Figures 6 and 7), with only four events being located outside this area. The depths of the 81 events ranged from 0.7 to 12.5 km, demonstrating that shallow seismicity dominates in the area. Three clusters were defined considering the spatial distribution of earthquakes and their focal mechanisms (Figure 6); these clusters will be described in section 5.2.

The moment magnitudes of earthquakes range between 2.1 and 4.1. Smaller events were detected (see Figure S5); however, these did not satisfy the location quality filtering criteria. Events in the western flank tend to have larger moment magnitudes than those in the eastern flank (Figures 5 and 6). However, no difference in magnitude was observed in the latitudinal direction.

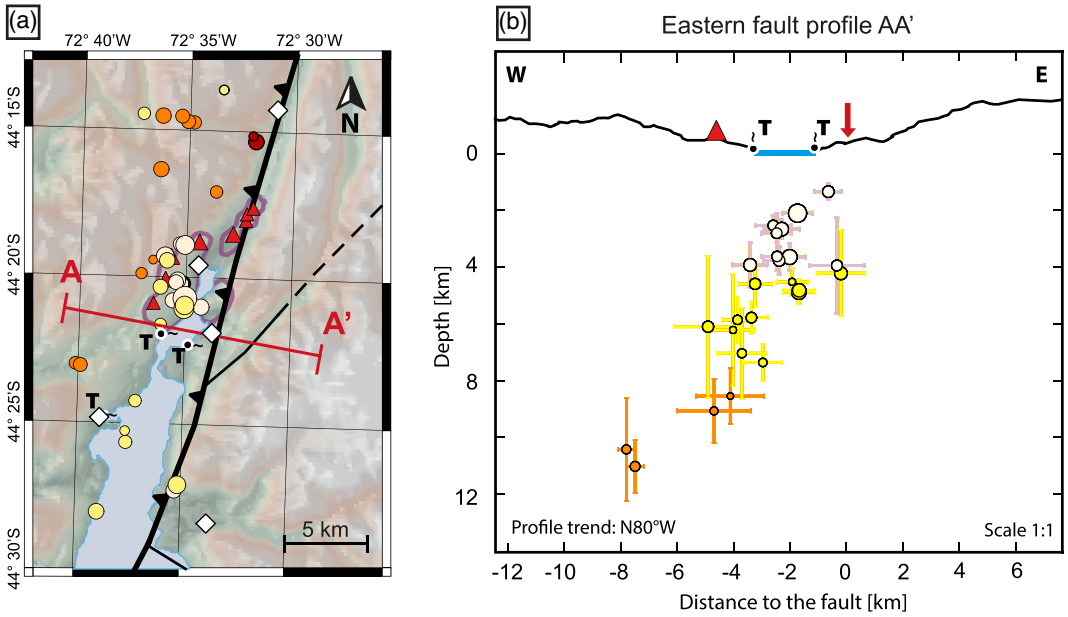

Figure 8. Cross-section of the eastern cluster. (a) A close-up of the cluster (location and legend in Figure 5). (b) Profile AA′, where error bars indicate the theoretical location errors in km. Distances were calculated using the translation and rotation coordinate transformation. The new coordinate system has its origin at the intersection between the fault and the profile and has a trend or rotation angle perpendicular to the fault strike (N10°E; Arancibia et al., 1999). Hence, zero distance and depth represent the intersection of the fault with the surface, and negative distances represent locations westward of the fault. The red arrow in (b) indicates the surface manifestation of the mapped fault. The topographic profile in (b) is drawn without vertical exaggeration, and the blue line represents the intersections of fjords with the profile. This profile section allows the fault dips to be inferred from the earthquakes by assuming that they occur in a similar fault plane.

Most of the focal mechanisms show strike-slip reverse or strike-slip normal kinematics (Figure 7b), while the second most common type of kinematics is normal strike-slip. Few dip-slip events occur, and these generally have some strike-slip component. Only one event had a purely dip-slip mechanism (M_w 3.8, Event 6; see Figure 7).

5.2. Seismic Clusters

Three main seismic clusters were identified, which we named the Eastern, Middle, and Western clusters (Figures 6 and 7). These three clusters are described in the following subsections. In each subsection, we describe the location, magnitude, and focal mechanisms of the events, as well as the spatial relationship between the events and nearby volcanic and geothermal features. The boundary between the Western and Middle clusters is not sharp, and we propose that this boundary could represent an intersection of faults. The two events that occurred in the intersection area were included in the Middle cluster as their focal mechanisms and depths are similar to those observed in the Middle cluster.

5.2.1. Eastern Cluster

The Eastern cluster, which is elongated in a NS direction, consists of a total of 35 events, with magnitudes ranging between M_w 2.1 and 3.5. The depths of these events ranged between 1.3 and 11 km; however, most were located between 2 and 8 km. Profile AA′, shown in Figure 8, suggests that this cluster has a west dipping distribution (~70°W).

The focal mechanisms of the Eastern cluster do not show a unique rupture mode (Figure 7b); however, most of the focal mechanisms indicate strike-slip reverse kinematics with one of the nodal planes striking N5° to 15°E (i.e., events 15, 17, 18, and 19). Structural evidence of NNE oriented right-lateral faulting in the same area (e.g., Arancibia et al., 1999) is consistent with the most common nodal planes of focal mechanisms in the Eastern cluster. Additionally, Event 15 documents reverse faulting, and an outlier focal mechanism in the northwestern segment of the cluster (Event 20 in Figure 7) shows EW oriented normal faulting.

The volcanic and geothermal features in the area of the Eastern cluster are the minor eruptive centers of the Puyuhuapi Volcanic Group, as well as two hot springs and one shallow well (which have surface water temperatures of 61°C, 50°C, and 86°C, respectively; Negri et al., 2018). The mean distance between any given earthquake of the Eastern cluster and a minor eruptive center is 4.4 km. A total of 21 events (60% of the cluster) were located less than 5 km from the Puyuhuapi Volcanic Group (Figure 8a).

5.2.2. Middle Cluster

The Middle cluster is located at Magdalena Island, consisting of 15 events with magnitudes ranging from M_w 2.4 to 4.1 and depths ranging from 3.8 to 11.6 km.

The focal mechanisms of this cluster suggest different kinematics but mainly vary between strike-slip and normal (Figure 7b). For the southern seismic events (see events 8 to 11 in Figure 7), we distinguish two kinds of focal mechanisms, namely (1) purely strike-slip (Events 8 and 10) and (2) normal strike-slip (Events 9 and 11). If all these focal mechanisms were on the same surface, this surface would be a NNE striking plane parallel to the Soto Sound lineament (Figure 7). One of the northern mechanisms (M_w 3.8, Event 6) is a seismological evidence of NE oriented normal faulting in the study area, as has been recorded in the northern and southern segments of the LOFS (Lange et al., 2008; Legrand et al., 2011; Russo et al., 2011).

The only volcanic feature in the vicinity of this cluster is the Mentolat stratovolcano (44.70°S/73.10°W; elevation: 1,660 m a.s.l.), which is located ~20 km south of the cluster and is formed from Pleistocene-to-Holocene basaltic andesites and andesitic lava flows (López-Escobar et al., 1993). The volume of this volcano has been estimated to be between 11 and 36.1 km^3 (Aravena, 2016; Völker et al., 2011).

5.2.3. Western Cluster

The Western cluster consists of a total of 15 events with magnitudes ranging between M_w 2.6 and 3.6, with a NNE trending epicentral distribution (see Figures 6 and S5). Earthquake depths ranging between 2.9 and 11.0 km. This cluster has a larger azimuthal gap than the others due to the distribution of the seismic network, and we therefore also used seismic data from a CSN station located in Chiloe Island (the northernmost station in Figure 1) to overcome the geometrical bias. The theoretical mean vertical and horizontal errors are 1.5 and 1.3 km, respectively, which are small considering the scale of the cluster, which covered an area of 50 × 20 km.

The focal mechanisms of the Western cluster are consistent with strike-slip reverse kinematics (events 1, 2, and 4 in Figure 7), all of which have a ~NS trending nodal solution. These kinematic agree with those of the Canal-Costa fault, which occurs to the south of the Western cluster and shows mostly oblique-slip ductile deformation (Cembrano et al., 2002). However, as was explained in section 4, these mechanisms have more uncertainties than other clusters (see Figure 7a). In the eastern part of the cluster, Event 5 shows different kinematics, mainly normal with a secondary strike-slip component; for that reason, it was included in the Middle cluster rather than the Western cluster.

No evidence of geothermal or volcanic features was found close to this cluster. The closest stratovolcano, Melimoyu Volcano, is located ~31 km from the cluster.

6. Discussion

6.1. Regional Observations

The first-order observation is that, of the focal mechanisms selected for discussion, 62% are strike-slip or strike-slip reverse/normal (see Figures 7b and 7c), 31% are normal or normal strike-slip, and only 6% (one event) is mainly reverse. These results suggest that current crustal deformation within the South American Plate along the volcanic arc is governed by faults with strike-slip kinematics. This is consistent with available long-term structural geological data from exhumed faults of the LOFS at this latitude (Arancibia et al., 1999; Lavenu & Cembrano, 1999) and along the entire LOFS (Lavenu & Cembrano, 1999; Pérez-Flores et al., 2016; Rosenau et al., 2006; Sielfeld et al., 2019).

Based on the geometry of mapped faults, the spatial distribution of epicenters, focal mechanisms, and geomorphological expression, most of the seismicity described in this study can be attributed to two NNE oriented right-lateral faults. These two master faults (or brittle deformation zones) are the likely sources of the Western and Eastern clusters, with most of the focal mechanisms in these two clusters presenting a NS to NNE oriented nodal plane solution. However, if the conjugate WNW oriented nodal planes of focal

mechanisms represent active faulting, such faults would occur as several individual discontinuities distributed within a length of 50 km. This scenario is inconsistent with the geomorphological lineaments and structural geological data (see Figure 2; Arancibia et al., 1999; Cembrano et al., 2002; Lavenu & Cembrano, 1999), and hence, our results are likely to be evidence of two N5°–15°E striking faults which represent the main seismogenic regional faults in the study area. Other regional interpretations for the Western cluster need to be tested using other independent data (e.g., from long GPS records, or a new seismic network with better coverage in the western area, between others); however, this is beyond the scope of this work. The western fault is known as the Canal-Costa fault and is the continuation of a ductile shear zone recognized to the south (Cembrano et al., 2002). No indicators of brittle kinematics (e.g., slickenlines on fault planes) have been reported on this fault from observations of the mesostructural geology. However, NS-oriented cataclastic rocks have been documented at ~46°S (Cembrano et al., 2002; Niemeyer et al., 1984). Additionally, a M_w 7.7, probably NS trending, dextral earthquake was recorded along the southern prolongation of the Canal-Costa fault on 6 June 1960 (Kanamori & Rivera, 2017; Figures 2 and S10). On the other hand, the eastern fault—which has previously been known as the Liquiñe-Ofqui fault (Ramos & Ghiglione, 2008; Thomson, 2002) or the Liquiñe-Ofqui fault zone (LOFZ) (Arancibia et al., 1999; Cembrano et al., 1996)—has well-known fault outcrops and produced shallow crustal earthquakes of the 2007 swarm (Vargas et al., 2013). To avoid confusion between the LOFS (a regional system of spatially and kinematically related faults) and the LOFZ (a single continuous fault zone), we locally refer to the eastern fault as the Puyuhuapi fault. Therefore, the Canal-Costa fault and the Puyuhuapi fault correspond to the two main regional master faults defining the Aysen strike-slip duplex (Cembrano et al., 1996).

6.2. Fault Geometry and Kinematics in the Aysen Duplex

In this subsection, we discuss details of the Puyuhuapi fault zone and the intraduplex domain in terms of fault geometries and kinematics. The Canal-Costa domain was not included since there are no reliable focal mechanisms to allow a novel discussion further than the above-mentioned spatial association between the western cluster and the previously documented brittle and ductile deformation. Conversely, for the Puyuhuapi fault zone and intraduplex domain, some novel interpretations can be made from the well-constrained focal mechanisms, as well as the seismicity distribution. We discuss the seismological observations, the mesostructural brittle faults, and the recorded ductile deformation; thereby, we finally describe the seismic productivity in terms of the number of earthquakes and their magnitude, and the volcanism, within both domains.

6.2.1. Puyuhuapi Fault Zone

The Puyuhuapi fault zone has a NNE elongated epicentral distribution along a length of at least 50 km. Based on the distribution of earthquake depths (Figure 8b), the Puyuhuapi fault zone can be inferred to dip ~70°W between the surface and ~12 km depth. Regarding the domain kinematics, most of the focal mechanisms are strike-slip reverse (Figures 7a and 7b) and the most common nodal solution is a N5–15° E-striking plane (e.g., Events 13, 15, 17, 18, and 19 in Figure 7). The ruptures recorded in focal mechanisms indicate a variable dip and prove that this fault zone can generate purely reverse earthquakes (Event 15) and earthquakes that are a mixture between right-lateral and reverse (Event 18). Variable dip and some oppositely striking planes (i.e., Mechanisms 16 and 21) suggest a deformation zone that involves more than a single fault (i.e., Hernandez-Moreno et al., 2014; with several block rotations). Considering the earthquake distribution, this fault zone may have a thickness of up to 10 km, half of which occurs to the north in the LOFS (Hernandez-Moreno et al., 2014) and concentrated to the west of the surface trace of the Puyuhuapi fault.

A previously published analysis of brittle faults in the Puyuhuapi fjord by Arancibia et al. (1999) is consistent with the existence of reverse and strike-slip faulting. Furthermore, a paleostress inversion shows that a transpressional regime has prevailed since the Pleistocene (~1.6 Ma from $^{40}Ar/^{39}Ar$ from biotites), which allows the coexistence of NS to NNE oriented right-lateral and reverse faults (Arancibia et al., 1999). Ductile deformation in the area is also consistent with the seismological observations made in the present study. Specifically, the Puyuhuapi Quarry shear zone shows a NNE striking, steeply dipping magmatic foliation and down-dip mineral lineations accompanied by outcrop-scale indicators such as the C/S fabrics of dextral-reverse ductile deformation (Cembrano et al., 2002; Figure 2). Similarities between long-term

ductile, brittle, and present-day shallow crustal seismicity suggest continuous protracted transpressional crustal deformation on the Puyuhuapi fault zone.

Regarding the seismic productivity, the Puyuhuapi fault zone is the most seismically active structure in this region, hosting most of the recorded earthquakes (47% of the total) and being associated with a lower moment release per event compared to the other fault domains (mean M_w ~ 2.7). The high seismic activity of this fault zone is also supported by the moderate-to-high slip rate of ~3.5 mm/yr that was estimated by Stanton-Yonge et al. (2016) using boundary element modeling. Other evidence of high activity along the Puyuhuapi fault is the young ductile deformation that is now exhumed and has been dated at 4 Ma (Cembrano et al., 2002). This ductile deformation is observable at the surface due to a high exhumation rate of ~2.5 to 3.3 mm/yr (and probably also a high rock uplift rate), that can be estimated assuming that the brittle-ductile transition is located at a depth of ~10–12 km, according to the depth of seismicity. Moreover, as described in section 5.2.1, all of the minor eruptive centers and most of the hot springs in the study area are spatially related to the Puyuhuapi fault zone, and a thermal anomaly has been inferred along this fault using fission-track thermochronology (Thomson, 2002). Thus, fluids and high temperature may influence, at least in part, the low magnitude and high recurrence rate of the seismic activity in this fault zone.

6.2.2. Intra-Duplex Domain

Along the intraduplex domain, focal mechanisms exhibit variable geometries and kinematics, varying from strike-slip to normal mechanisms (Figures 7a and 7b). Shallow crustal earthquakes are widespread along this domain, and thus several concealed and outcropping faults are expected. However, considering that there are few documented surface faults within this domain, we cannot associate the intra-duplex seismicity with any specific outcropping fault. Nevertheless, it is remarkable that several focal mechanisms show normal or strike-slip normal ruptures (Figure 7b). Regarding the orientation of the normal faults, only Event 6 has a single nodal plane striking solution, namely, N69°E. Most other normal mechanisms are consistent with NE or WNW orientations (e.g., Events 3, 5, 9, and 11). Numerous NE oriented normal and dextral-normal faults have been observed along the SVZ (e.g., Cembrano & Lara, 2009; Pérez-Flores et al., 2016; Rosenau et al., 2006; Vargas et al., 2013; Villalobos et al., 2020), and similar focal mechanisms were detected during the 2007 Aysen swarm (Legrand et al., 2011; Russo et al., 2011). In particular, NE oriented faults and NE oriented lineaments have been found to be kinematically coupled with volcanoes and some of the minor eruptive centers located in the SVZ (Cembrano & Lara, 2009). Hence, considering Event 6 and the structural observations along the SVZ, NE oriented faulting seems to be the most appropriate solution for the normal kinematics in the intra-duplex domain, although, with the available information, we cannot discard a WNW-oriented normal solution.

No mesostructural brittle fractures have been documented inside this area, probably due to the low accessibility of most offshore outcrops. However, north of Melimoyu volcano, NS oriented strike-slip faults and NE oriented normal faults have been mapped crosscutting Miocene-to-Pliocene intrusive rocks (Mella & Páez, 2011; Figure 7). Mella and Páez (2011) also reported a NS oriented normal-dextral fault ~20 km in length along the Yanteles–Melimoyu fault zone. These observations were made far from the seismicity presented in this work—at least ~20 km—and thus, the seismicity is not clearly related to these previously documented faults. The ductile deformation of this domain is restricted to the Canal-Jacaf shear zone, where there is a NS oriented subvertical mylonitic foliation with a poorly defined down-dip stretching lineation; however, outcrop-scale observations suggest a dextral-reverse displacement (Cembrano et al., 2002).

Regarding the seismic productivity of the intraduplex domain, 38% of the seismicity is accumulated with a mean magnitude of $M_w = 2.9$. Major stratovolcanoes are located within the duplex, and thus the faulting in this area may be relevant for understanding their emplacement (see section 6.4).

6.3. Tectonic Model and its Regional Consistency With Previous Works

Here, we present a conceptual tectonic model of the brittle crustal deformation within the SVZ constrained to the region between 43°50′ and 45°00′S. This model captures both the instantaneous deformations reflected by our novel seismological data, and the long-term deformation recorded in structural geology measurements (Arancibia et al., 1999; Cembrano et al., 2002). The presented model constitutes a conceptual framework approximating the governing tectonic processes in the SVZ, which by nature have a complex evolution in time and space (e.g., Bonali et al., 2015; Hobbs et al., 2019; LaFemina et al., 2005;

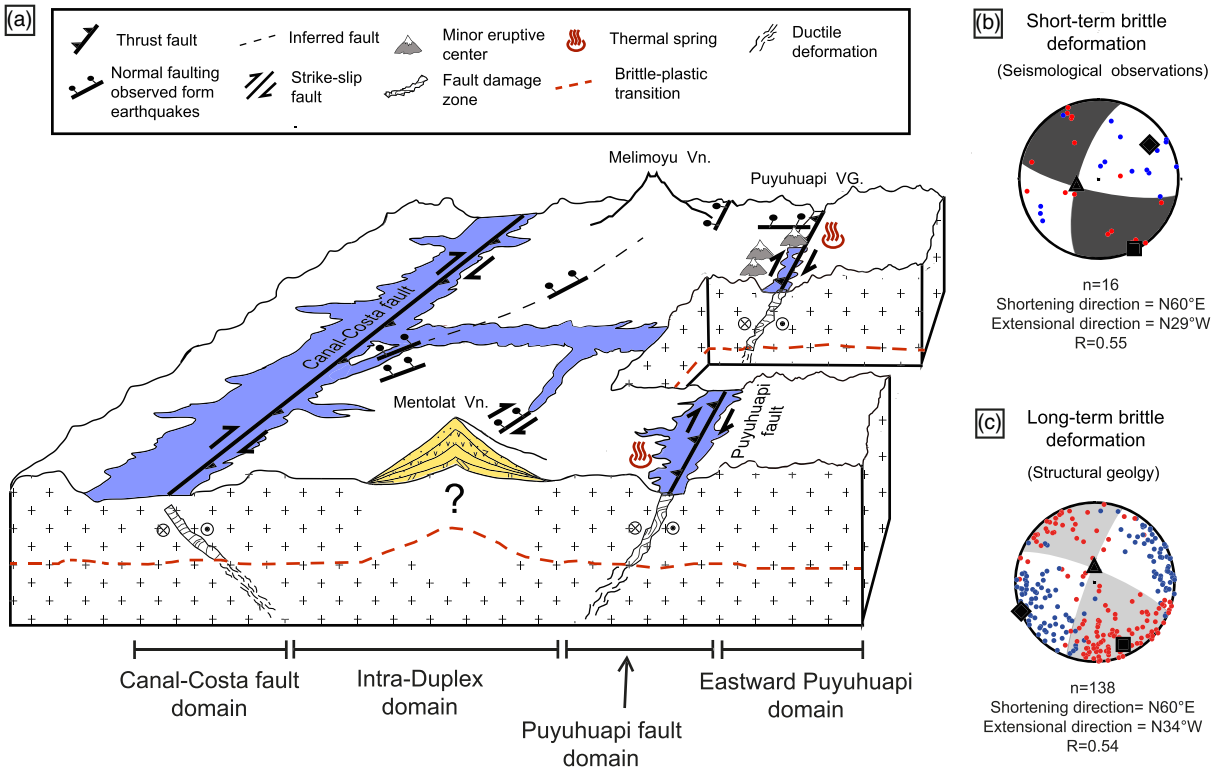

Figure 9. (a) Tectonic model of the study area based on earthquake locations and focal mechanisms determined in the present study and the discussion in sections 6.1 and 6.2, shown together with the structural geology of exhumed faults (Arancibia et al., 1999) and ductile kinematics (Cembrano et al., 2002). Dark yellow symbolizes volcanic lava strata and blue symbolizes water bodies (e.g., fjords and sounds). The red dashed line represents the approximate location of the brittle-ductile transition (~11 km depth). (b) Directions of regional shortening and extension calculated from the 15 selected focal mechanisms of this study using the statistical Bingham distribution in the FaultKin software (Allmendinger et al., 2012; Marrett & Allmendinger, 1990). Blue and red dots show the P and T directions of each event, respectively. (c) Directions of regional shortening and extension calculated from the seven mesostructural sites of Arancibia et al. (1999). Blue and red dots represent the P and T direction of each fault slip data, respectively. In (b) and (c), black diamonds, triangles, and squares represent the regional strain directions of E_1, E_2, and E_3, respectively, where E_1, E_2, and E_3 are the eigenvalues of the Bingham moment tensor; n represents the number of data; and $R = (E_2 - E_3)/(E_1 - E_3)$.

Stanton-Yonge et al., 2016). In particular, the conditions presented in this model are indicative of long-term intra-plate behavior.

The proposed model represents the continental-scale fault architecture of a duplex with two main NNE oriented master faults, separated by ~60 km with dextral to dextral-reverse kinematics (Figure 9a). Based on the 15 focal mechanisms accepted in section 4, the mean shortening direction of the area is N60°E/18° and the mean extension direction is N151°E/03° (Figure 9b). This model is consistent with the duplex configuration proposed by previous authors (e.g., Cembrano et al., 1996, 2002; Hervé, 1994). However, some details are not entirely consistent with the positive-flower model suggested by Ramos and Ghiglione (2008) and Thomson (2002), in which master faults are joined in the brittle-plastic transition. None of the recorded earthquakes in the present support such joining in the brittle-plastic transition and no focal mechanisms from the deeper zones of the faults show listric behavior. Furthermore, most of the focal mechanics presented here have subvertical planes, suggesting several separated subvertical fault arrangements which accommodate strike-slip deformation. This difference can be explained by one of the following possibilities: (1) the small time window used in the present study means that insufficient seismicity is collected to shed light on these listric/curve brittle faults or (2) this joining occurs, but is located in the lower ductile crust.

In our tectonic model, we simplified most of the normal kinematics in the intraduplex domain to NE oriented faults or ruptures. However, several explanations for normal faulting can be evaluated: (1) NE oriented normal faulting in Event 6 due to a continuous dextral deformation (Figure 10a); (2) WNW oriented normal faulting due to a rotation of the shortening direction (Figure 10b); or (3) a complex deformation

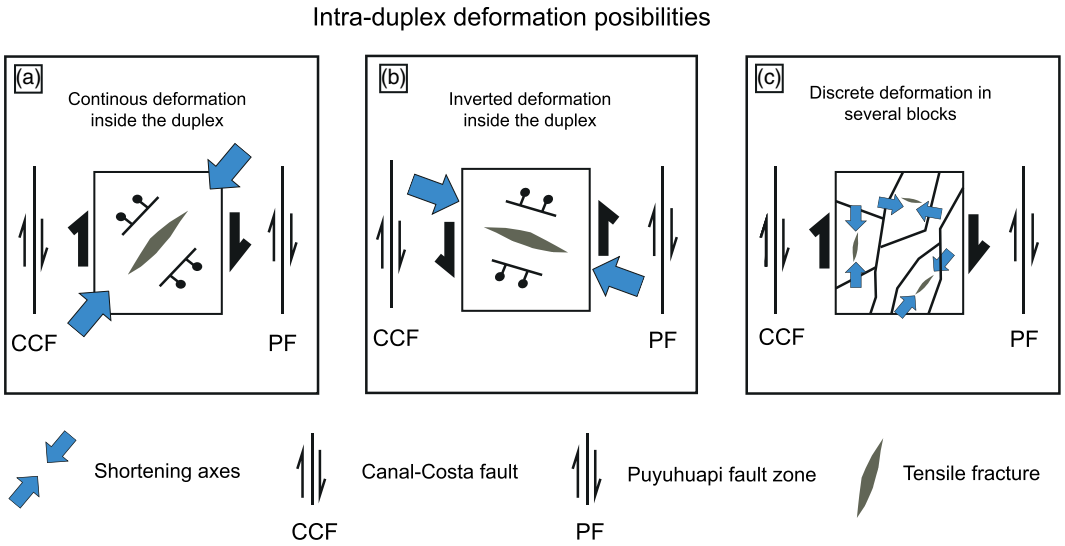

Figure 10. Different deformation (a. continuous, b. inverted, c. discrete) processes that can explain the normal faulting inside the duplex. See text for further details of the reliability of each deformation process.

process which includes several rotated blocks and their particular shortening and extension directions (Figure 10c). Only possibility (2) can be discarded since there is no regional horizontal rotation of the *P* and *T* directions inside the duplex (Figure 11). We prefer solution (1) instead of (3) since the first solution is consistent with previous observations in the area (Cembrano & Lara, 2009; Iturrieta et al., 2017; Rosenau et al., 2006; Vargas et al., 2013) and the only normal event with a clearly striking rupture plane (Event 6). Besides, a similar tectonic setting has been observed in real cases, for example, the prevalence of normal faulting between the San Jacinto and Coyote creek faults—two strike-slip reverse faults in California which could be analogous to the Canal-Costa and Puyuhuapi faults (Nicholson et al., 1986). To perform an evaluation of Hypothesis (3), further work must be done, such as a widespread analysis of magnetic rotation vectors (e.g., Hernandez-Moreno et al., 2014) or decades of seismic and GPS observations. Additionally, some vertical rotation of the *P* axis is observed in the intraduplex domain (Figures 7b and 11), which suggests that the height of the volcanic edifice and/or the upward intrusion of laccolite may increase the vertical stress (e.g., Van Wyk de Vries & Merle, 1998; Turcotte & Schubert, 2014), stimulating normal faulting.

Comparing our model with the documented seismicity, the same fault geometry and kinematics are observed in the north (Lange et al., 2008) and south (2007 Aysen swarm; Agurto et al., 2012; Legrand et al., 2011; Russo et al., 2011) of the study area. According to these authors, right-lateral NNW to NNE trending faulting accompanied by NE trending normal to normal right-lateral faulting has been interpreted as the predominant faulting type. The differences between the seismicity recorded in this work and the previously documented seismicity can be summarized as follows. Between 41° and 43°S, only one main NS-oriented master fault of the LOFS (as well as several secondary faults) have been documented (Lange et al., 2008), suggesting that the duplex configuration does not extend to the north of the study area. Conversely, to the south of the study area, the events of the 2007 Aysen swarm reveal the main NS oriented fault associated with the Puyuhuapi fault (Agurto et al., 2012; Legrand et al., 2011). Additionally, Kanamori and Rivera (2017) showed three events with magnitudes of M_w 5.0, 5.2, and 7.7, which can be attributed to the Canal-Costa fault (see Figure 2). Thus, the duplex configuration can be expected to extend at least until the epicentral location of 45°42′S (Kanamori & Rivera, 2017) to the south of the study area and until 44°S (Events 1 and 2 in this paper) to the north.

Our tectonic model is consistent with the elastoplastic model proposed by Iturrieta et al. (2017) in terms of geometry and kinematics, and our work partially validates the fault geometry proposed by these authors. The first-order similarities between our model and that of Iturrieta et al. (2017) are as follows: (1) the fault geometry; (2) the fact that the main NS oriented faults, such as the Canal-Costa and Puyuhuapi faults,

Features	Canal-Costa fault	Intra-duplex domain	Puyuhuapi fault zone	Eastward Puyuhuapi domain
Type of volcanism	No evidence	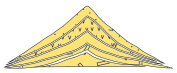 Stratovolcanoes 2 cones (Melimoyu & Mentolat) 71 - 174 km^3 of lava	 Minor eruptive centers 9 cones ~ 1 km^3 of lava	No evidence
Composition of volc. rocks	-	Dacite, Andesite and Basalt	Basalt	-
Short-term brittle deformation (seismological observations)	Uncertain data	 n=8 R=0.31 P-direction = 054°/66° T-direction = 151°/03° B-direction = 242°/23°	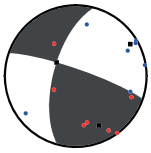 n=7 R=0.74 P-direction = 060°/11° T-direction = 155°/24° B-direction = 305°/63°	No data
Seismological kinematics	Uncertain data	Normal Normal strike-slip Strike-slip - normal	Strike-slip reverse Strike-slip Reverse	-
Long-term brittle deformation (structural geology)	No data	No data	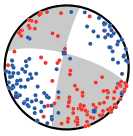 n=99 R=0.53 P-direction = 240°/07° T-direction = 148°/18° B-direction = 350°/70°	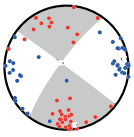 n=39 R=0.55 P-direction = 081°/06° T-direction = 172°/07° B-direction = 312°/80°
Brittle tectonic regime	-	Transtension	Transpression Strike-slip	Strike-slip

Figure 11. Table showing the main differences in volcanism and tectonic settings in the study area (each domain is defined in Figure 9a). The volcanic edifice volume was estimated from Aravena (2016) and Völker et al. (2011). Seismological beachballs were calculated from the *P* and *T* directions of focal mechanisms using the Bingham statistical method in the FaultKin software (Allmendinger et al., 2012). *R* is the strain ellipsoid shape ratio described in the text, according to Diraison et al. (2000) and Pérez-Flores et al. (2016). Long-term brittle deformation was obtained from the fault slip data of Arancibia et al. (1999). The Puyuhuapi fault domain was calculated from brittle deformation Sites 1, 2, 3, and 7 (see Figure 2), and the eastern Puyuhuapi domain was calculated from brittle deformation Sites 4, 5, and 6. The brittle tectonic regime was defined based on the values of *R*.

have a transpressional regime, as inferred by the stress shape ratio (Iturrieta et al., 2017) and supported by the focal mechanisms presented in our study (Figures 7 and 11); and (3) the stress shape ratio of elastoplastic modeling and focal mechanisms suggest that NE oriented faults inside the duplex should have a transtensional stress regime (Figure 11). However, there are differences between the reverse-slip behavior predicted by Iturrieta et al. (2017) and seismicity presented in this work, namely that the seismicity presented here suggests that reverse-faulting behavior is concentrated in the Puyuhuapi fault, whereas the elastoplastic modeling of Iturrieta et al. (2017) predicts that thrusting will be concentrated in the Canal-Costa fault. Despite these differences, the similarity between both works supports the results of the elastoplastic modeling as a predictor of the brittle crust deformation.

The brittle structural geology of the study area documented by previous authors (Arancibia et al., 1999; Lavenu & Cembrano, 1999) shows similar patterns to the measured seismicity at a regional scale (see Figures 9b and 9c). Most of the exhumed faults are NNE oriented right-lateral faults, such as our inferred Puyuhuapi fault. Paleo-stress inversion suggests that a transpressional regime with a shortening direction of N60°E has existed in the study region since ~1.6 Ma (Arancibia et al., 1999; Lavenu & Cembrano, 1999, Figure 9c). The shortening direction calculated using the *P* and *T* vectors of all the seismic events analyzed in the present study is equal (N60°E, Figure 9b), suggesting the continuity of the stress regime since the Quaternary.

Additionally, ductile deformation recorded by Cembrano et al. (2002) also shows similar patterns to the seismicity and the model presented in the present study, as reflected by the four studied shear zones (see Figure 2): (1) the Puyuhuapi Quarry shear zone in the Puyuhuapi fjord shows reverse and right-lateral deformation (Cembrano et al., 2002), consistent with Events 13 to 19 in the present study (Figure 7); (2) the Canal-Jacaf shear zone has right-lateral kinematics, consistent with the kinematics observed for Events 8–11 a few kilometers to the south (see Figure 7). However, there are differences in the observed dip-slip component, since according to focal mechanisms dip-slip component may be normal, otherwise according to ductile deformation in Canal-Jacaf dip-slip component may be reverse; (3) the Canal-Costa shear zone provides the main published structural geological evidence of the Canal-Costa fault and reflects a NNE oriented right-lateral fault with reverse kinematics. Seismicity presented here, also suggests strike-slip reverse kinematics on Canal-Costa fault (i.e., Events 1 and 2) but with a low confidence, as was discussed in section 4; and (4) the Rio Cisne shear zone displays NE-oriented right-lateral normal deformation, similar to that suggested by the N69°E striking nodal planes of Event 6, among other events. Finally, ductile deformation has been dated at ~4 Ma (Cembrano et al., 2002) based on the $^{40}Ar/^{39}Ar$ dating of biotite and muscovite. Accordingly, ductile deformation, brittle faulting, and seismicity suggest that the regional stress field and fault kinematics have been relatively constant since ~4 Ma. The similarity between the ductile and brittle behavior in this area indicates that the shear deformation process is not restricted to the upper crust, but rather extends to the brittle and ductile crust with a similar strike and dip (consistent with the shear zone model of Scholz (1988)).

6.4. Spatial Correlation Between Volcanoes, Faulting, and Tectonic Settings

To better understand the faults and tectonic characteristics that are spatially associated with the different types of volcanism in the study area, we divided the tectonic model into four areas from west to east: (1) the Canal-Costa fault domain; (2) the intraduplex domain; (3) the Puyuhuapi fault zone domain; and (4) eastward of the Puyuhuapi fault (Figure 9a). For each area, we will summarize the type and volume of volcanic edifices (the latter as a proxy to estimate eruptive rates), seismic data, and the available mesostructural geological data (Figure 11) to discuss the tectonic regime and its implications for magma transport through the crust.

The volume of volcanic edifices differs significantly between the four domains. In the Canal-Costa domain, there is no evidence of volcanism. In the intraduplex domain, two large stratovolcanoes are identified: Melimoyu, with a volume of ~60–142 km^3, and Mentolat, with a volume of ~11–36 km^3 (Aravena, 2016; Völker et al., 2011). Geoffroy et al. (2018) calculated non-DRE tephra volumes of ~2.6 and ~1.6 km^3 related to two closely spaced Holocene explosive eruptions at Melimoyu. Phenocryst thermobarometry of these events suggests magma residency at moderately shallow sub-volcanic depths (>8.5 km; Geoffroy et al., 2018). The eruptive style, magma volume, and extrusion rate in this domain suggest the presence of a local favorable tectonic condition for magma emplacement and transportation to the surface. In this domain lava composition varies between dacite, andesite, and basalt considering the Mentolat and Melimoyu volcanos (López-Escobar et al., 1993; Naranjo & Stern, 2004). In the Puyuhuapi fault domain, there are nine minor eruptive centers aligned with the Puyuhuapi fault with a combined volcanic edifice volume of ~1.2 km^3 (Völker et al., 2011). Minor eruptive centers are commonly formed by short-lived multiple eruption phases (e.g., Brand & White, 2007; Houghton & Schmincke, 1989) and their occurrence suggests relatively low rates of magma supply (Takada, 1994) when are compared to the stratovolcanoes. The seismogenic Puyuhuapi fault, which controls the distribution of minor eruptive centers, could facilitate the direct transport to the surface of basaltic magmas that originated in the mantle and experienced differentiation processes

that included at least olivine fractionation (Lahsen et al., 1994). In the eastern domain, no volcanism has been identified.

Regarding the tectonic regime, transtension and transpression can be inferred from the strain ellipsoid obtained from the analysis of seismicity and brittle faults, which is available for the three eastern domains (Figure 11). According to the seismic observations in this study, the intraduplex domain is dominated by a transtensional tectonic environment ($R = 0.31$); the Puyuhuapi fault domain, which has a low eruptive rate, is dominated by a transpressional environment ($R = 0.74$), as documented by previous authors (Arancibia et al., 1999; Cembrano et al., 2002); meanwhile, the eastern domain has a strike-slip regime ($R = 0.55$), as supported by the structural geological data (Figure 11). Additionally, the tectonic regimes of different domains are consistent with the faulting mode observed from seismicity; that is, in the intraduplex domain varying from normal to strike-slip and in the Puyuhuapi fault zone domain varying from strike-slip to reverse (Figure 11). Regarding the *P* direction, it is remarkable that the focal mechanisms of the intraduplex domain have a more vertical shortening direction than those of the other domains (Figures 7b and 11).

Considering previous models linking volcanism with tectonics in the SVZ, several declare that NE oriented faults are the easiest pathways for magma ascent (Cembrano & Lara, 2009; López-Escobar et al., 1995; Nakamura, 1977; Pérez-Flores et al., 2016; Rosenau et al., 2006; Sánchez et al., 2013) since these faults are perfectly oriented to develop dilatational fractures (e.g., Cox, 2005; Hill, 1977; Scholz, 2002, Figure 10a). Similar observations have been made from theoretical and analogous models (Van Wyk de Vries & Merle, 1998), in which graben formation parallel to the shortening direction was observed close to volcanic edifice.

In the present study, we propose a NE orientation as the preferred solution for normal faulting, which is almost parallel to the regional-scale shortening direction (Figures 9b and 9c) and remains constant for each domain (see the *P* direction in Figure 11, which varies between N54°E and N81°E). Therefore, the seismological observations from the southern tip of the SVZ presented in this work agree with the dilatation fractures hypothesis, based on the short-term brittle deformation. Additionally, focal mechanisms indicate a vertical rotation of the *P* shortening axis inside the duplex, which can be stimulated by the upward intrusion of laccolites and the increase of vertical height due to volcanoes (Turcotte & Schubert, 2014; Van Wyk de Vries & Merle, 1998), thus promoting the formation of normal faults (i.e., the Yanteles-Melimuyu fault zone). The upward intrusion of laccolites and volcanic height may also increase $\sigma 2$ and E_2, since both are vertical in the study are; consequently, E_2 get similar to E_1 promoting a local transtension. Thus, the combination of laccolite intrusions, the increasing height of volcanoes, and NE trending faults can explain the fact that the largest extruded lava volume is concentrated in a local transtensional area where dilatational fractures may occur. There, the presence of dilatational fractures and this particular tectonic setting may also permit a wide range of magma compositions varying between basalt, andesite, and dacite (Mentolat and Melimoyu volcanoes), much more variable than the exclusively basaltic magma observed along the transpressional NS oriented Puyuhuapi fault. Notably, in the study area, the transtensional environment occurs in certain areas within the strike-slip and/or transpressional domains defined by the main NS oriented faults, which are oriented perpendicular to the direction of the subduction of the Nazca Plate beneath the South American Plate.

Nevertheless, the emplacement of volcanoes cannot be attributed only to the NE oriented faulting. This is due to the fact that, although these dilatational fractures allow an easy path for magma ascent, such ascent does not necessarily lead to magma emplacement and accumulation. Fault interaction may also be an important factor in volcano emplacement, as has been discussed by other authors (e.g., Iturrieta et al., 2017; Pérez-Flores et al., 2016; Sánchez et al., 2013). Additionally, even with the new seismic data and recompilation of structural geology information presented in this study, the fault continuity and attitude inside the duplex cannot be completely resolved. Thus, further effort must be made to identify the specific fault settings below the stratovolcanoes in the study area. For example, using local structural geology in the vicinity of volcanic edifices or deploying a longer-term seismic network (with a duration of at least a decade). However, despite the uncertainty in fault interactions, it is remarkable that higher volcanic edifice volume, high eruptive rates, and variable magma composition can be found in (1) a local transtensional tectonic environment with (2) a *P* axis that is more vertical than those in the other domains (Figure 7b) and with (3) NE oriented normal or partially normal faulting, as suggested by numerous seismological evidences. In contrast, in

transpressional environments, such as the NNE oriented Puyuhuapi fault, only basalts with small volcanic edifice volume and low extrusion rate are observed, suggesting a less productive magma transportation process.

7. Conclusions

We deployed a temporary seismic network for 10 months between August 2016 and May 2017. In this period, we recorded more than 200 seismic events. Eighty-one of these events passed our location-quality filter (location errors less than 3.5 km, RMS less than 0.3 s, more than six stations with clear records of *P* and *S* wave phases, and azimuthal gap below 240°), and these were selected for further analysis. The magnitudes of the selected events ranged between M_w 2.1 and 4.1 and their depths varied between 0.7 and 12.5 km. The main conclusions of this work are as follows:

1. The spatial distribution and kinematics of the events shows that most of the seismicity can be attributed to two parallel, NNE oriented master faults with dextral to dextral-reverse kinematics separated by ~60 km. Both faults are consistent with the geometry of mapped faults. These two main faults (the Puyuhuapi and Canal–Costa faults) generate a duplex configuration which controls the continental-scale fault settings between at least 44° and 45°30′S.
2. At the regional scale, the *P* and *T* axes of all focal mechanisms are consistent with a strike-slip regime with a N60°E/18°E shortening direction and a N151°E/03°S extensional direction. Our results are coherent with the Quaternary (~1.6 Ma) stress regime calculated from exhumed faults (Arancibia et al., 1999). Most interestingly, our results are also consistent with long-term ductile deformation for the Puyuhuapi and Canal-Costa faults documented by Cembrano et al. (2002), dated at ~4 Ma. This long-term ductile deformation suggests an unchanged transpressional regime since ~4 Ma along the Puyuhuapi fault zone. Additionally, the similarity in the fault strike and fault kinematics between both deformation processes (brittle and ductile) reveals a crustal-scale shear deformation occurring along the brittle and ductile crust.
3. Inside this duplex, widespread normal to strike-slip normal faulting can be inferred from earthquake focal mechanisms. It is remarkable that, inside the duplex, local transtension dominates and major stratovolcanoes are emplaced.
4. Our results suggest that the emplacement of stratovolcanoes—which implies the ascent of large volumes of magma—is spatially related to normal faulting in a local transtensional environment inside the duplex. Conversely, all minor eruptive centers in the study area—with low volume of magma extruded—are spatially associated with the Puyuhuapi fault zone in a transpressional environment at the eastern edge of the duplex. Generally, for the whole SVZ and locally in the study area, NE trending faults are perfectly oriented to develop dilatational fractures since they are subparallel to the local and regional shortening direction. These faults would allow a higher magma flux through the crust in comparison with the master NNE to NS trending strike-slip reverse faults of the LOFS.

Acknowledgments

This is a contribution to the ANID-Project #15090013 Centro de Excelencia en Geotermia de los Andes (CEGA). This work was partially funded by the project BIP30346723-0 "Estimación y valorización del potencial geotérmico de Aysén" BIP30346723-0 and the project BIP 40010311 "Factibilidad de cogeneración geotérmica en Puyuhuapi". Seismic stations were provided by the Pontifical Catholic University of Chile. We thank the inhabitants of Puyuhuapi (Don Florentino, Don Ramón, José Nahuelquín, Ramon Carcher, and the Puyuhuapi Lodge), and CONAF for allowing the installation of the seismic stations. We also thank Daniel Basualto and the Observatorio Volcanológico de los Andes del Sur (OVDAS) for providing us with the data from the permanent seismic stations and helping to develop this study. We also offer thanks to Helena Azócar, Iván Garrido, Valeria Salas, and Pamela Sepúlveda for their help with the detection of seismic events, and to Sebastián Carrasco of the CSN for kind discussion. We finally thank Pablo Iturrieta for his clarifying discussions. Tomás Roquer acknowledges financial support from the ANID doctoral grant #21171178. Finally, we thank Dr. José Martínez-Díaz, as well as the anonymous reviewer and both associate editors, for their useful comments which allowed us to increase the quality of this work.

Data Availability Statement

The location, date, and other details of the earthquakes (Class A and Class B events) can be found in the Zenodo repository (https://doi.org/10.5281/zenodo.3472066). Details of the network installation, HypoDD results, and focal mechanisms can be found in the supporting information in Microsoft Word format.

References

Agurto, H., Rietbrock, A., Barrientos, S., Bataille, K., & Legrand, D. (2012). Seismo-tectonic structure of the Aysén region, Southern Chile, inferred from the 2007 M_w = 6.2 Aysén earthquake sequence. *Geophysical Journal International*, *190*(1), 116–130. https://doi.org/10.1111/j.1365-246X.2012.05507.x

Allmendinger, R., Cardozo, N., & Fisher, D. (2012). *Structural geology algorithms: Vectors and tensors*. Cambridge, England: Cambridge University Press. https://doi.org/10.1017/CBO9780511920202

Alvarez-Gomez, J. A. (2019). FMC—Earthquake focal mechanisms data management, cluster and classification. *SoftwareX*, *9*, 299–307. https://doi.org/10.1016/j.softx.2019.03.008

Arancibia, G., Cembrano, J., & Lavenu, A. (1999). Transpresión dextral y partición de la deformación en la Zona de Falla Liquiñe-Ofqui, Aisén, Chile (44-45°S). *Revista Geologica de Chile*, *26*(1), 3–22. https://doi.org/10.4067/S0716-02081999000100001

Aravena, D. (2016). Balance Comparativo de volumenes de edificions volcánicos en la zona volcánica sur. Ms. Sc Geology Thesis. Universidad de Chile.

Bai, L., Wu, Z., Zhang, T., & Kawasaki, I. (2006). The effect of distribution of stations upon location error: Statistical tests based on the double-difference earthquake location algorithm and the bootstrap method. *Earth, Planets and Space*, *58*(2), e9–e12. https://doi.org/10.1186/BF03353364

Bonali, F. L., Tibaldi, A., & Corazzato, C. (2015). Sensitivity analysis of earthquake-induced static stress changes on volcanoes: The 2010 *Mw* 8.8 Chile earthquake. *Geophysical Journal International*, *201*(3), 1868–1890. https://doi.org/10.1093/gji/ggv122

Bondár, I., Myers, S. C., Engdual, E. R., & Bergman, E. A. (2004). Epicenter accuracy based on seismic network criteria. *Geophysical Journal International*, *156*(3), 483–496. https://doi.org/10.1111/j.1365-246X.2004.02070.x

Brand, B. D., & White, C. M. (2007). Origin and stratigraphy of phreatomagmatic deposits at the Pleistocene sinker Butte volcano, western Snake River Plain, Idaho. *Journal of Volcanology and Geothermal Research*, *160*(3–4), 319–339. https://doi.org/10.1016/j.jvolgeores.2006.10.007

Cembrano, J., Hervé, F., & Lavenu, A. (1996). The Liquiñe Ofqui fault zone: A long-lived intra-arc fault system in southern Chile. *Tectonophysics*, *259*(1-3), 55–66. https://doi.org/10.1016/0040-1951(95)00066-6

Cembrano, J., & Lara, L. (2009). The link between volcanism and tectonics in the southern volcanic zone of the Chilean Andes: A review. *Tectonophysics*, *471*(1–2), 96–113. https://doi.org/10.1016/j.tecto.2009.02.038

Cembrano, J., Lavenu, A., Reynolds, P., Arancibia, G., López, G., & Sanhueza, A. (2002). Late Cenozoic transpressional ductile deformation north of the Nazca–South America–Antarctica triple junction. *Tectonophysics*, *354*(3–4), 289–314. https://doi.org/10.1016/S0040-1951(02)00388-8

Cole, J. W. (1990). Structural control and origin of volcanism in the Taupo volcanic zone, New Zealand. *Bulletin of Volcanology*, *52*(6), 445–459. https://doi.org/10.1007/BF00268925

Corti, G., Carminati, E., Mazzarini, F., & Mo, G. (2005). Active strike-slip faulting in El Salvador, Central America. *Geology*, *33*(12), 989–992. https://doi.org/10.1130/G21992.1

Cox, S. F. (2005). Coupling between deformation, fluid pressures, and fluid flow in ore-producing hydrothermal systems at depth in the crust. In *100th Anniversary Volume* (pp. 39–75). USA: Society of Economic Geology.

DeMets, C., Gordon, R. G., & Argus, D. F. (2010). Geologically current plate motions. *Geophysical Journal International*, *181*(1), 1–80. https://doi.org/10.1111/j.1365-246X.2009.04491.x

Dewey, J., Holdsworth, R., & Strachan, R. (1998). *Transpression and transtension zones*, *Special Publications* (Vol. 135, pp. 1–14). London: Geological Society. https://doi.org/10.1144/GSL.SP.1998.135.01.01

Dewey, J. W., Herron, E., & Kork, J. O. (1999). Recent calibration events in the United States. In *21st Seismic research symposium* (pp. 48–57). Las Vegas, Nevada, USA.

Diraison, M., Cobbold, P., Gapais, D., Rossello, E., & Le Corre, C. (2000). Cenozoic crustal thickening, wrenching and rifting in the foothills of the southernmost Andes. *Tectonophysics*, *316*(1–2), 91–119. https://doi.org/10.1016/S0040-1951(99)00255-3

Faulkner, D. R., Jackson, C. A. L., Lunn, R. J., Schlische, R. W., Shipton, Z. K., Wibberley, C. A. J., & Withjack, M. O. (2010). A review of recent developments concerning the structure, mechanics and fluid flow properties of fault zones. *Journal of Structural Geology*, *32*(11), 1557–1575. https://doi.org/10.1016/j.jsg.2010.06.009

Geoffroy, C. A., Alloway, B. V., Amigo, À., Parada, M. A., Gutierrez, F., Castruccio, A., et al. (2018). A widespread compositionally bimodal tephra sourced from Volcán Melimoyu (44°S, northern Patagonian Andes): Insights into magmatic reservoir processes and opportunities for regional correlation. *Quaternary Science Reviews*, *200*, 141–159. https://doi.org/10.1016/j.quascirev.2018.09.034

Giambiagi, L., Álvarez, P. P., Creixell, C., Mardonez, D., Murillo, I., Velásquez, R., & Barrionuevo, M. (2017). Cenozoic shift from compression to strike-slip stress regime in the high Andes at 30°S, during the shallowing of the slab: Implications for the El Indio/Tambo mineral district. *Tectonics*, *36*, 2714–2735. https://doi.org/10.1002/2017TC004608

Gudmundsson, A. (2011). *Rock fractures in geological processes*. New York: Cambridge University Press. https://doi.org/10.1017/CBO9780511975684

Hanks, T. C., & Kanamori, H. (1979). A moment magnitude scale. *Journal of Geophysical Research*, *84*(B5), 2348–2350. https://doi.org/10.1029/JB084iB05p02348

Harland, W. B. (1971). Tectonic transpression in Caledonian Spitsbergen. *Geological Magazine*, *108*(1), 27–41. https://doi.org/10.1017/S0016756800050937

Havskov, J., & Ottemöller, L. (2010). *Routine data processing in earthquake seismology* (p. 1–347). Berlin: Springer. ISBN: 978-90-481-8696-9. https://doi.org/10.1007/978-90-481-8697-6

Hernandez-Moreno, C., Speranza, F., & Di Chiara, A. (2014). Understanding kinematics of intra-arc transcurrent deformation: Paleomagnetic evidence from the Liquiñe-Ofqui fault zone (Chile, 38–41° S). *Tectonics*, *33*, 1964–1988. https://doi.org/10.1002/2014TC003622

Hervé, F. (1994). The Southern Andes between 39° and 44°S latitude: The geological signature of a transpressive tectonic regime related to a magmatic arc. In *Tectonics of the Southern Central Andes* (pp. 243–248). Berlin: Springer. https://doi.org/10.1007/978-3-642-77353-2_17

Hill, D. (1977). A model of earthquake swarms. *Journal of Geophysical Research*, *82*(8), 1347–1352. https://doi.org/10.1029/JB082i008p01347

Hobbs, T. E., Newman, A. V., & Protti, M. (2019). Enigmatic upper-plate sliver transport paused by megathrust earthquake and afterslip. *Earth and Planetary Science Letters*, *520*, 87–93. https://doi.org/10.1016/j.epsl.2019.05.016

Houghton, B. F., & Schmincke, H. U. (1989). Rothenberg scoria cone, east Eifel: A complex Strombolian and phreatomagmatic volcano. *Bulletin of Volcanology*, *52*(1), 28–48. https://doi.org/10.1007/BF00641385

Ingebritsen, S., & Gleeson, T. (2017). Crustal permeability. *Hydrogeology Journal*, *25*(8), 2221–2224. https://doi.org/10.1007/s10040-017-1663-4

Iturrieta, P., Hurtado, D., Cembrano, J., & Stanton-Yonge, A. (2017). States of stress and slip partitioning in a continental scale strike-slip duplex: Tectonic and magmatic implications by means of finite element modeling. *Earth and Planetary Science Letters*, *473*, 71–82. https://doi.org/10.1016/j.epsl.2017.05.041

Kanamori, H., & Rivera, L. (2017). An *Mw* = 7.7 slow earthquake in 1960 near the Aysén Fjord region, Chile. *Geophysical Journal International*, *211*(1), 93–106. https://doi.org/10.1093/GJI/GGX292

Kaverina, A. M., Lander, A. V., & Prozorov, A. G. (1996). Global creepex distribution and its relation to earthquake-source geometry and tectonic origin. *Geophysical Journal International*, *125*(1), 249–265. https://doi.org/10.1111/j.1365-246X.1996.tb06549.x

Kim, Y. S., Peacock, D., & Sanderson, D. (2004). Fault damage zones. *Journal of Structural Geology*, *26*(3), 503–517. https://doi.org/10.1016/j.jsg.2003.08.002

LaFemina, P. C., Connor, C. B., Hill, B. E., Strauch, W., & Armando Saballos, J. (2004). Magma-tectonic interactions in Nicaragua: The 1999 seismic swarm and eruption of Cerro Negro volcano. *Journal in Volcanology and Geothermal Research*, *137*(1–3), 187–199. https://doi.org/10.1016/j.jvolgeores.2004.05.006

LaFemina, P. C., Dixon, T. H., Malservisi, R., Árnadóttir, T., Sturkell, E., Sigmundsson, F., & Einarsson, P. (2005). Strain partitioning and accumulation in a propagating ridge system: Geodetic GPS measurements in South Iceland. *Journal of Geophysical Research*, *110*, B11405. https://doi.org/10.1029/2005JB003675

LaFemina, P. C., Dixon, T. H., & Strauch, W. (2002). Bookshelf faulting in Nicaragua. *Geology*, *30*(8), 751–754. https://doi.org/10.1130/0091-7613(2002)030<0751:BFIN>2.0.CO;2

Lahsen, A., López-Escobar, L., & Vergara, M. (1994). The Puyuhuapi volcanic group, Southern Andes (44°20′S): Geological and geochemical antecedents. In *VII Congreso Geológico Chileno* (pp. 1076–1079). Concepción, Chile: VII Congreso Geológico Chileno.

Lamur, A., Kendrick, J., Eggertsson, G. J., Wall, R. D., Ashworth, J., & Lavallée, Y. (2017). The permeability of fractured rocks in pressurised volcanic and geothermal systems. *Scientific Reports*, 6173. https://doi.org/10.1038/s41598-017-05460-4

Lange, D., Cembrano, J., Rietbrock, A., Haberland, C., Dahm, T., & Bataille, K. (2008). First seismic record for intra-arc strike-slip tectonics along the Liquiñe–Ofqui fault zone at the obliquely convergent plate margin of the southern Andes. *Tectonophysics*, *455*(1–4), 14–24. https://doi.org/10.1016/j.tecto.2008.04.014

Lavenu, A., & Cembrano, J. (1999). Compressional- and transpressional-stress pattern for Pliocene and quaternary brittle deformation in fore arc and intra-arc zones (Andes of Central and Southern Chile). *Journal of Structural Geology*, *21*(12), 1669–1691. https://doi.org/10.1016/S0191-8141(99)00111-X

Legrand, D., Barrientos, S., Bataille, K., Cembrano, J., & Pavez, A. (2011). The fluid-driven tectonic swarm of Aysen Fjord, Chile (2007) associated with two earthquakes ($Mw = 6.1$ and $Mw = 6.2$) within the Liquiñe–Ofqui Fault zone. *Continental Shelf Research*, *31*(3–4), 154–161. https://doi.org/10.1016/j.csr.2010.05.008

Lienert, B. (1994). HYPOCENTER 3.2: A computer program for locating earthquakes locally, regionally and globally.

López-Escobar, L., Cembrano, J., & Roa, H. (1995). Geochemistry and tectonics of the Chilean Southern Andes basaltic quaternary volcanism (37–46°S). *Andean Geology*, *22*(2), 219–234. https://doi.org/10.5027/andgeoV22n2-a06

López-Escobar, L., Kilian, R., Kempton, P., & Tagiri, M. (1993). Petrography and geochemistry of quaternary rocks from the southern volcanic zone of the Andes between 41°30′ and 46°00′S, Chile. *Revista Geologica de Chile*, *20*(1), 33–35. https://doi.org/10.5027/andgeoV20n1-a04

Marrett, R., & Allmendinger, R. (1990). Kinematic analysis of fault-slip data. *Journal of Structural Geology*, *12*(8), 973–986. https://doi.org/10.1016/0191-8141(90)90093-E

Mella, M., & Páez, D. (2011). Mapa Geología base área Puerto Raúl Marín Balmaceda, Región de Aysén. Servicio Nacional de Geología y Mineria, Escala 1:50.000.

Mella, M., Ramos, A., Kraus, S., & Duhart, P. (2012). Datos tefroestratigráficos de erupciones Holocenas del Volcán Mentolat, Andes del Sur (44°40' S), Chile. *Resumenes Expandidos, XIII Congreso Geológico Chileno. Antofagasta, Chile, August 201*.

Melnick, D., Bookhagen, B., Strecker, M., & Echtler, H. (2009). Segmentation of megathrust rupture zones from fore-arc deformation patterns over hundreds to millions of years, Arauco peninsula, Chile. *Journal of Geophysical Research*, *114*, B01407. https://doi.org/10.1029/2008JB005788

Melnick, D., Rosenau, M., Folguera, A., & Echtler, H. (2006). Neogene tectonic evolution of the Neuquén Andes western flank (37–39°S. *Geological Society of America Special Paper*, *407*, 73–95). https://doi.org/10.1130/2006.2407(04)

Michael, A. J. (1984). Determination of stress from slip data: Faults and folds. *Journal of Geophysical Research*, *89*(B13), 11,517–11,526. https://doi.org/10.1029/JB089iB13p11517

Michael, A. J. (1987). Use of focal mechanisms to determine stress: A control study. *Journal of Geophysical Research*, *92*(B1), 357–368. https://doi.org/10.1029/JB092iB01p00357

Mogi, K. (1967). Earthquakes and fractures. *Tectonophysics*, *5*(1), 35–55. https://doi.org/10.1016/0040-1951(67)90043-1

Mooney, W., Prodehl, C., & Pavlenkova, N. (2002). Seismic velocity structure of the continental lithosphere from controlled source data. *International Geophysics*, *81*, 887–910. https://doi.org/10.1016/S0074-6142(02)80261-3

Mora, C., Comte, D., Russo, R., Gallego, A., & Mocanu, V. (2010). Aysén seismic swarm (January 2007) in southern Chile: Analysis using joint hypocenter determination. *Journal of Seismology*, *14*(4), 683–691. https://doi.org/10.1007/s10950-010-9190-y

Nakamura, K. (1977). Volcanoes as possible indicators of tectonic stress orientation—Principle and proposal. *Journal of Volcanology and Geothermal Research*, *2*(1), 1–16. https://doi.org/10.1016/0377-0273(77)90012-9

Naranjo, J. A., & Stern, C. R. (2004). Holocene tephrochronology of the southernmost part (42°30′–45° S) of the Andean southern volcanic zone. *Revista Geologica de Chile*, *31*(2), 224–240.

Negri, A., Daniele, L., Aravena, D., Muñoz, M., Delgado Huertas, A., & Morata, D. (2018). Decoding fjord water contribution and geochemical processes in the Aysen thermal springs (southern Patagonia, Chile). *Journal of Geochemical Exploration*, *185*, 1–13. https://doi.org/10.1016/j.gexplo.2017.10.026

Nicholson, C., Seeber, L., Williams, P., & Syles, L. R. (1986). Seismic evidence for conjugate slip and block rotation within the San Andreas fault system, southern California. *Tectonics*, *5*(4), 629–648. https://doi.org/10.1029/TC005i004p00629

Niemeyer, H., Skarmenta, J., Fuenzalida, R., & Espinoza, W. (1984). Hojas Península de Taitao y Puerto Aisén. Servicio Nacional de Geología y Mineria, Carta Geológica Chile, Nos. 60–61.

Obstubo, M., Yamaji, A., & Kubo, A. (2008). Determination of stresses from heterogeneous focal mechanism data: An adaptation of the multiple inverse method. *Tectonophysics*, *457*, 150–160.

Ottermöller, L., Voss, P., & Havskov, J. (2014). Seisan earthquake analysis software for Windows, Solaris, Linux and Macosx. http://seisan.info

Pardo-Casas, F., & Molnar, P. (1987). Relative motion of the Nazca (Farallon) and south American plates since late cretaceous time. *Tectonics*, *6*(3), 233–248. https://doi.org/10.1029/TC006i003p00233

Pérez-Flores, P., Cembrano, J., Sánchez, P., Veloso, E., Arancibia, G., & Roquer, T. (2016). Tectonics, magmatism and paleo-fluid distribution in a strike-slip setting: Insights from the northern termination of the Liquiñe–Ofqui fault system, Chile. *Tectonophysics*, *680*, 192–210. https://doi.org/10.1016/j.tecto.2016.05.016

Pérez-Flores, P., Wang, G., Mitchell, T. M., Meredith, P., Nara, Y., Sarkar, V., & Cembrano, J. (2017). The effect of offset on fracture permeability of rocks from the Southern Andes volcanic zone, Chile. *Journal of Structural Geology*, *104*, 142–158. https://doi.org/10.1016/j.jsg.2017.09.015

Petit, J. P. (1987). Criteria for the sense of movement on fault surfaces in brittle rocks. *Journal of Structural Geology*, *9*(5–6), 597–608. https://doi.org/10.1016/0191-8141(87)90145-3

Quinteros, J., & Sobolev, S. (2013). Why has the Nazca plate slowed since the Neogene? *Geology*, *41*(1), 31–34. https://doi.org/10.1130/G33497.1

Radic, J. (2010). Las cuencas cenozoicas y su control en el volcanismo de los Complejos Nevados de Chillan y Copahue-Callaqui (Andes del Sur, 36–39°S). *Andean Geology*, *37*(1), 220–246. https://doi.org/10.4067/S0718-71062010000100009

Ramos, V., & Ghiglione, M. (2008). Tectonic evolution of the Patagonian Andes. *Developments in Quaternary Sciences*, *11*, 57–71. https://doi.org/10.1016/S1571-0866(07)10004-X

Rivera, O., & Cembrano, J. (2000). Modelo de formación de cuencas volcano-tectónicas en zonas de transferencia oblicuas a la cadena andina: El caso de las cuencas Oligo-Miocenas de Chile central y su relación con estructuras NWW-NW (33°00′-34°30′). *In 9th Chilean Geological Congress*.

Rosenau, M., Melnick, D., & Echtler, H. (2006). Kinematic constraints on intra-arc shear and strain partitioning in the southern Andes between 38°S and 42°S latitude. *Tectonics*, *25*, TC4013. https://doi.org/10.1029/2005TC001943

Rowland, J., & Sibson, R. (2004). Structural controls on hydrothermal flow in a segmented rift system, Taupo volcanic zone, New Zealand. *Geofluids*, *4*(4), 259–283. https://doi.org/10.1111/j.1468-8123.2004.00091.x

Russo, R. M., Gallego, A., Comte, D., Mocanu, V. I., Murdie, R. E., Mora, C., & VanDecar, J. C. (2011). Triggered seismic activity in the Liquiñe–Ofqui fault zone, southern Chile, during the 2007 Aysen seismic swarm. *Geophysical Journal International*, *184*(3), 1317–1326. https://doi.org/10.1111/j.1365-246X.2010.04908.x

Sánchez, P., Pérez-Flores, P., Arancibia, G., Cembrano, J., & Reich, M. (2013). Crustal deformation effects on the chemical evolution of geothermal systems: The intra-arc Liquiñe–Ofqui fault system, Southern Andes. *International Geology Review*, *55*(11), 1384–1400. https://doi.org/10.1080/00206814.2013.775731

Scholz, C. (1988). The brittle-plastic transition and depth of seismic faulting. *Geologische Rundschau*, *77*(1), 319–328. https://doi.org/10.1007/BF01848693

Scholz, C. (2002). *The mechanics of earthquake faulting* (2nd ed.). Cambridge: Cambridge University Press. https://doi.org/10.1017/CBO9780511818516

SERNAGEOMIN (2003). *Mapa Geológico de Chile: versión digital*, *Publicación Geológica Digital* (Vol. 4). Santiago, Chile: Servicio Nacional de Geología y Mineria de Chile.

Sielfeld, G., Lange, D., & Cembrano, J. (2019). Intra-Arc Crustal Seismicity: Seismotectonic Implications for the Southern Andes Volcanic Zone, Chile. *Tectonics*, *38*, 552–578. https://doi.org/10.1029/2018TC004985

Stanton-Yonge, A., Griffith, W., Cembrano, J., St. Julien, R., & Iturrieta, P. (2016). Tectonic role of margin-parallel and margin-transverse faults during oblique subduction in the southern volcanic zone of the Andes: Insights from boundary element modeling: Slip partitioning southern Andes. *Tectonics*, *35*, 1990–2013. https://doi.org/10.1002/2016TC004226

Stern, C., De Porras, M., & Maldonado, A. (2015). Tephrochronology of the upper Río Cisnes valley (44°S), southern Chile. *Andean Geology*, *42*(2), 173–189. https://doi.org/10.5027/andgeoV42n2-a02

Takada, A. (1994). The influence of regional stress and magmatic input on styles of monogenetic and polygenetic volcanism. *Journal of Geophysical Research*, *99*(B7), 13,563–13,573. https://doi.org/10.1029/94JB00494

Thomson, S. (2002). Late Cenozoic geomorphic and tectonic evolution of the Patagonian Andes between latitudes 42°S and 46°S: An appraisal based on fission-track results from the transpressional intra-arc Liquiñe–Ofqui fault zone. *Geological Society of America Bulletin*, *114*(9), 1159–1173. https://doi.org/10.1130/0016-7606(2002)114<1159:LCGATE>2.0.CO;2

Turcotte, D. L., & Schubert, G. (2014). *Geodynamics* (3° ed., *Cap.3*). Cambridge: Cambridge University Press.

Van Wyk de Vries, B., & Merle, O. (1998). Extension induced by volcanic loading in regional strike-slip zones. *Geology*, *26*(11), 983–986. https://doi.org/10.1130/0091-7613(1998)026<0983:EIBVLI>2.3.CO;2

Vargas, G., Rebolledo, S., Sepulveda, S. A., Lahsen, A., Thiele, R., Townley, B., et al. (2013). Submarine earthquake rupture, active faulting and volcanism along the major Liquiñe–Ofqui Fault Zone and implications for seismic hazard assessment in the Patagonian Andes. *Andean Geology*, *40*, 141–171.

Villalobos, A., Easton, G., Maksymowicz, A., Ruiz, S., Lastras, G., De Pascale, G.P., & Agurto-Detzel, H. (2020). Active faulting, submarine surface rupture, and seismic migration along the Liquiñe-Ofqui Fault System, Patagonian Andes. *Journal of Geophysical Research: Solid Earth*, *125*, e2020JB019946. https://doi.org/10.1029/2020JB019946

Völker, D., Kutterolf, S., & Wehrmann, H. (2011). Comparative mass balance of volcanic edifices at the southern volcanic zone of the Andes between 33°S and 46°S. *Journal of Volcanology and Geothermal Research*, *205*(3–4), 114–129. https://doi.org/10.1016/j.jvolgeores.2011.03.011

Waldhauser, F. (2001). HypoDD: A computer program to compute double-difference earthquake locations. *U. S. Geological. Survey Open-File Rep., 01–113*.

Waldhauser, F., & Ellsworth, W. L. (2000). A double-difference earthquake location algorithm: Method and application to the northern Hayward Fault, California. *Bulletin of the Seismological Society of America*, *90*(6), 1353–1368. https://doi.org/10.1785/0120000006

Yamaji, A. (2000). The multiple inverse method: A new technique to separate stresses from heterogeneous fault-slip data. *Journal of Structural Geology*, *22*(4), 441–452. https://doi.org/10.1016/S0191-8141(99)00163-7